IMAGE SEGMENTATION, PARAMETRIC STUDY, AND SUPERVISED SURROGATE MODELING OF IMAGE-BASED COMPUTATIONAL FLUID DYNAMICS

by

Md Mahfuzul Islam

A Thesis

Submitted to the Faculty of Purdue University

In Partial Fulfillment of the Requirements for the degree of

Master of Science in Mechanical Engineering

Department of Mechanical and Energy Engineering at IUPUI

Indianapolis, Indiana

May 2022

THE PURDUE UNIVERSITY GRADUATE SCHOOL
STATEMENT OF COMMITTEE APPROVAL

Dr. Huidan (Whitney) Yu, Chair
Department of Mechanical and Energy Engineering

Dr. Xiaoping Du
Department of Mechanical and Energy Engineering

Dr. Diane Wagner
Department of Mechanical and Energy Engineering

Approved by:
Dr. Jie Chen

To my honorable parents and beloved brother

ACKNOWLEDGMENTS

First, I would like to thank my thesis supervisor, Dr. Huidan (Whitney) Yu, for allowing me to be involved in this research and for her continuous guidance, cooperation, motivation, and support throughout the completion of my thesis. I found her as a person of immense knowledge and capable of critical problem-solving. I want to thank her for keeping faith in me during my tough times in research and keeping me motivated until the end of my thesis. I am also incredibly grateful to Dr. Xiaoping Du for his kind input and guidance and for allowing me to audit his classes to support my research. I am thankful to my lab-mates, Xiaoyu Zhang, Weichen Hong, and John Talamantes, for their valuable time and support towards my research. Xiaoyu assisted me in starting my research and gave me ideas about several useful software packages to execute different purposes. I got immense help from her during the computational model setup, debugging, and validation. I also want to thank Huiru Li for her tremendous support and collaboration in my research. I am also grateful to my dear friends Radhika Bhaumik and Rabiul Hasan. They were always there for me and kept me motivated during the tough times. I am also thankful to my parents and young brother for their support and sacrifices to help me pursue my dream. Without their continuous encouragement, this accomplishment would have never come true.

TABLE OF CONTENTS

LIST OF TABLES

LIST OF FIGURES

SYMBOLS

m	mass
v	velocity
P	pressure
t	time
P_s	mean pressure gradient
P_0	fluctuation of pulsatile pressure gradient
ω	angular frequency
μ	kinematic viscosity
ρ	density
u	velocity
α	Womersley number
V_{sys}	peak systolic velocity
V_{edv}	end-of-diastolic velocity
N_D	number of cells or grids in diameter
S_D	diameter reduction
S_V	volume reduction

ABBREVIATIONS

ICFD Image-based Computational Fluid Dynamics

VLBM Volumetric Lattice Boltzmann Method

RI Resistive Index

CFD Computational Fluid Dynamics

CTA Computed Tomography Angiogram

MRI Magnetic Resonance Imaging

DUS Doppler Ultrasound Sonography

WNS Wall Normal Stress

WSS Wall Shear Stress

4-D Four Dimension

3-D Three Dimension

CT Computed Tomography

SEM Scanning Electron Microscope

CAD Computer-Aided Design

LBM Lattice Boltzmann Method

NS Navier-Stokes

GPU Graphics Processing Unit

ML Machine Learning

STL Standard Triangle Language

RGB Red Green Blue

GP Gaussian Process

GPR Gaussian Process Regression

DACE Design and Analysis of Computer Experiments

PSV Peak Systolic Velocity

EDV End Diastolic Velocity

HR Heart Rate

CHD Computational Hemodynamics

BC Boundary Condition

ABSTRACT

With the recent advancement of computation and imaging technology, Image-based computational fluid dynamics (ICFD) has emerged as a great non-invasive capability to study biomedical flows. These modern technologies increase the potential of computation-aided diagnostics and therapeutics in a patient-specific environment. I studied three components of this image-based computational fluid dynamics process in this work.

To ensure accurate medical assessment, realistic computational analysis is needed, for which patient-specific image segmentation of the diseased vessel is of paramount importance. In this work, image segmentation of several human arteries, veins, capillaries, and organs was conducted to use them for further hemodynamic simulations. To accomplish these, several open-source and commercial software packages were implemented.

This study incorporates a new computational platform, called *InVascular*, to quantify the 4D velocity field in image-based pulsatile flows using the Volumetric Lattice Boltzmann Method (VLBM). We also conducted several parametric studies on an idealized case of a 3-D pipe with the dimensions of a human renal artery. We investigated the relationship between stenosis severity and Resistive index (RI). We also explored how pulsatile parameters like heart rate or pulsatile pressure gradient affect RI.

As the process of ICFD analysis is based on imaging and other hemodynamic data, it is often time-consuming due to the extensive data processing time. For clinicians to make fast medical decisions regarding their patients, we need rapid and accurate ICFD results. To achieve that, we also developed surrogate models to show the potential of supervised machine learning methods in constructing efficient and precise surrogate models for Hagen-Poiseuille and Womersley flows.

1. INTRODUCTION

Computational fluid dynamics (CFD) has become a pillar for scientific and engineering discoveries complementing experimental analysis. CFD is diversely used in the vast arena of research and engineering problems in many sectors of study and industries. Lately, CFD is also being used to study biological flow[1,2] and is making an essential contribution to medical research in designing implantable products, like, stents[3] and ventricular assist devices[4] and in predicting function, as in the cardiovascular[5] and respiratory systems.[6,7]

With the recent development in radiological imaging such as Computed tomography angiogram (CTA)/Magnetic resonance imaging (MRI) and Doppler ultrasound sonography (DUS), image processing, and computational techniques, patient-specific computational modeling of vascular hemodynamics from image data has emerged as a handy tool with the prospects of improved clinical care. Thus, Image-based computational fluid dynamics (ICFD) has become a new capability in the biomedical and clinical research field in understanding the underlying mechanisms of vascular diseases like stenosis, aneurysms, etc., and thus might be a vital tool in clinical decision-making.[7]

1.1 Image-based Computational Fluid Dynamics for Medical Applications

Although CFD began its development with the dawn of the digital computer in the early 1950s [8,9], ICFD has emerged[10-16] relatively recently as a new computer-aided tool for diagnostics and therapeutics of cardiovascular diseases with the advances in medical imaging, scientific modeling, and computational power. Based on medical imaging data, such as CTA or MRI, together with DUS, ICFD has enabled the non-invasive evaluation of 4-D in vivo vectorial velocity in the entire arterial system with satisfactory spatial and temporal resolution.

Pulsatile flow is common in the cardiovascular system, and its flow domain geometry is exceptionally complicated. A typical pulsatile flow is four-dimensional (4-D: 3-D in space plus 1-D in time). These flows consist of a positive mean and a periodically varying time-dependent component around the mean. The wall stresses, wall-normal stress (WNS), and wall-shear stress (WSS) play central roles in aneurysm initiation, growth, and rupture[17] and the development of atherosclerosis[18].

Wall stresses for cardiovascular hemodynamics can be fully characterized based on their topological, spatiotemporal, and vectorial nature[18,19], which remains problematic in ICFD due to the fact that the natural human vasculature is typical of irregular geometry and orientation with curvatures and bifurcations. In contrast to traditional vascular assessments, complex hemodynamics can be assessed by ICFD blood flow simulations. Determining which metrics can help us predict disease development and progression has become the predominant discussion.[20] ICFD has become a mainstay in studying cardiovascular diseases like stenosis and aneurysms for many other reasons. The narrowing of the arteries causes stenosis in the process of atherosclerosis over time. It is a significant cause of illness and death globally. On the other hand, an aneurysm is a bulge or rapid expansion in the wall of an artery. ICFD for a cerebral aneurysm using the patient-specific geometry model was first reported by DA Steinman et al. in 2003[21]. This information shows that fluid dynamics of blood flow, or hemodynamics, contribute significantly to understanding the pathology caused by aneurysms, including their initiation, growth, and rupture.[22-26]

Atherosclerotic plaques are commonly seen at arterial bifurcations and bends. This observation has helped us universally conclude that local hemodynamic factors, particularly wall shear stresses (WSS), play a significant role in the initiation of the disease or, perhaps, more importantly, in the progression.[27,28] But measuring wall shear stress, the force exerted by flowing blood on the vessel wall, in vivo-is very challenging.[29] With the union of high-performance desktop workstations and high-resolution medical imaging, it is possible to create realistic ICFD models of intact vessels. The hemodynamic factors of interest can be easily extracted.[27,30]

Moreover, streamlines and pathlines provide a visual demonstration of flow through 3-dimensional (3D) structures and are the mainstay option in ICFD; they are of utmost importance for surgeons to see changes in flow patterns caused by procedures that alter local anatomy. Furthermore, ICFD gives flow velocities and pressures that are helpful in objective decision-making. For example, based on Bernoulli's equation, velocity carries vast importance in clinical applications. Instead, it is often used to quantify flow, pressure, or the cross-sectional area of a structure through which blood flows.[31] Thus, a higher velocity means the passage of blood through a narrower scope or stenosed vessel. Thus, ICFD allows for a non-invasive way of investigating several critical clinical questions and not previously possible at a level of detail. ICFD analysis

also simulates and predicts the hemodynamics and outcome of intervention during virtual surgery.[32,33]

Apart from blood flow simulation, ICFD can also be implemented to simulate airflow in the vocal tract and respiratory organs. Although respiratory diseases account for millions of deaths worldwide,[34] typical diagnostic techniques are inconsistent with early pathophysiological changes in lung function. They do not always match with the patient's symptoms and outcomes.[35] On the other hand, ICFD that could predictively estimate a known clinical measure and still provide regional information would prove to be a promising tool for clinical decision-making. Moreover, in contrast to experimental flow studies, it is trivial to alter model parameters such as flow rates, wall properties, etc. This has made ICFD a particularly attractive tool for hemodynamics research.[27]

1.2 Image Data to 4-D Fluid Dynamics

In practice, A typical case of ICFD consists of three essential components:

1. 3-D anatomical extraction for the morphology of the diseased vessel from medical image data or construction of 3-D geometry in CAD software for idealized assumptions.

2. Quantification of 4-D fluid dynamics employing physical parameters together with initial and boundary conditions based on DUS. Conducting validation to ensure physical accuracy of results. Post-processing with parametric study, statistical analysis, and the cognizance of the primary reasons for the disease progression and subsequent physiological response.

3. Ensuring computational efficiency to get the results as they will help medical professionals and patients make decisions regarding treatment and therapeutics.

The details of each step are largely problem-specific but share many standard features.[32] The discussion below will focus mainly on aspects common to VLBM in modeling basic fluid flow while also bringing out some unique considerations relevant to ICFD research.

1.2.1 rocesses from Medical Images to 3-D flow domains

There are three types of medical image data involved in this study that we used for anatomical extraction or 3D reconstruction of the vessel of interest and for conducting fluid dynamic analysis: CTA/ MRI, SEM, DUS. Image data from CTA/MRI, and SEM were used for

image segmentation and 3-D reconstruction of the vessel of interest for ICFD analysis. DUS images were not used for image segmentation in this study. We used it for setting up the inflow boundary conditions for the parametric study.

Computed tomography (CT) scan is a form of x-ray that uses a computer to take cross-sectional images of the human body. Computed tomography angiography (CTA) combines a CT scan with a special dye or contrast material in order to create images of blood vessels and tissues in a section of the body. An MRI scan uses a large magnet, radio waves, and a computer to create a detailed, cross-sectional image of internal organs and structures. Although the imaging technology behind CTA and MRI images are quite different, in both cases, the images come in the same DICOM (Digital Imaging and Communications in Medicine) format. So, the image segmentation procedure to extract the vessel of interest from these image data is remarkably similar.

Scanning electron microscope (SEM) is an electron microscope that scans the surface of a sample with a focused beam of electrons and produces images. SEM does optical sectioning of the vessel of interest and provides images in 8-bit/16-bit RGB format usually.

CTA, MRI, and DUS are on the macro-scale, and all of them are used for medical diagnosis and research. SEM images are in the micro-scale and used only for research currently, not for medical diagnosis. The resolution for these SEM images is extremely high, whereas the resolution of CTA, and MRI images, is not so much. CTA and MRI images come in 3D volumetric forms so that we may have 50, 100, 200, or even more 2-D image slices from three different axes going through the vessel or organ of interest. When combined, these image slices form a 3-D volume of the scanned body. For SEM, we just get one or two image slices that can show the high-resolution cross-section of the choriocapillaris and the opening of the arteries and venules to that vascular layer.

In this research, an open-source software package, 3D Slicer, was used for image segmentation from CT/MRI images and for creating a 3D reconstruction of the vessel of interest. We used MATLAB for the image processing and 3-D construction of the choroid layer from SEM image data. Also, for idealized assumptions, commercial Computer-Aided Design (CAD) software packages, Siemens NX, and SolidWorks were incorporated.

1.2.2 Validation and Parametric Study

Due to the restriction of computational power and time, only a part of vessel anatomy is included in ICFD, and thus boundary conditions must be applied at inlets and outlets of the segmented vessel to accurately depict the vascular network outside of the local domain. The introduction of inlet BC is quite simple, imposing either a parabolic flow profile based on the Poiseuille solution to the flow in a circular pipe or using the analytical solution for Womersley flow in a pipe based on a velocity wave from DUS measurement. The choice of outflow BC in ICFD is diverse, including zero pressure or zero traction conditions, resistance or impedance conditions, and reduced-order models, which can be an open or closed-loop or reduced-order one-dimensional wave propagation equations.[36-38 39,40] One other class of ICFD methods for simulating complex flows is the Lattice Boltzmann method (LBM). Instead of directly solving a set of nonlinear partial differential equations, i.e., Navier-Stokes (NS) equations, LBM uses a discretized kinetic model on a regular lattice six to recreate the dynamic of inexpressible fluid flow, in which the non-linearity is separated from the non-locality. Thus due to its particulate nature and local dynamics, the LBM has several advantages over the NS-based ICFD method, especially in dealing with complex boundaries,[41,42] incorporating microscopic interactions[1,43] in multiphase flows, and implementing Graphics processing unit (GPU) parallelization of the algorithm.[1,41,43,44] In this work, we used a unique computational platform developed in our lab over the years that we call *InVascular*, for quantifying the 4-D velocity field in image-based pulsatile flows by using a volumetric lattice Boltzmann method (VLBM).[42]

Ensuring physical accuracy and, at the same time achieving computational efficiency remains challenging in ICFD since the real human vascular system is usually irregular in geometry and orientation. When the artery is diseased with either stenosis (lumen reduction) or aneurysm (lumen enlargement), its geometry can be extremely difficult. For these reasons, a more idealized geometry can be used for conducting parametric studies and exploring the underlying flow physics.

To determine appropriate spatial resolution convergence check was done, and numerical results were compared against analytical results obtained from the Womersley solution for Pulsatile flow. To conduct the parametric study, we created an idealized geometry, a 3-D pipe with the exact dimensions of a renal artery, and we varied the heart rate and pulsatile pressure gradient, respectively, to see their effects on Resistive index (RI). RI is defined as (peak systolic velocity – end-diastolic velocity) / peak systolic velocity in the cortex or medulla of the kidney. Also, stenosis

was created inside the pipe geometry, and the severity was varied to investigate how that affects the RI.

1.2.3 Machine Learning for Efficient ICFD

Machine learning (ML) is the use of data and algorithms to imitate the way that humans learn, gradually improving its accuracy. It is a data analysis method that teaches computers to do what humans and animals do naturally: learn from the experience. Machine learning algorithms use computational approaches to "learn" information straight from data without resorting to a predefined equation as the model. The algorithms adaptively enhance their performance as the number of samples data available for learning increases. It has broad applications in prediction, image recognition, speech recognition, medical diagnoses, the financial industry, and trading. Nowadays, machine learning is being implemented in many sectors of scientific research.

In numerous scientific fields, the main objective is to find out the correlation between a set of detectable quantities (inputs) and another set of variables that are related to these (outputs). Once such a mathematical model is set, predicting the value of the desired variables by measuring the observables becomes possible. Regrettably, many real-world phenomena are too complicated to model as a direct closed-form input-output relationship. Machine learning provides methods that can automatically create a computational model of these complex relations by processing the available data and exploiting a problem-dependent performance standard. This process of the model building automatically is called "training," and the available data used for these training purposes is called "training data." This trained model now can provide new insights into how input variables are mapped to the output, and it can also be used to make predictions for novel input values that were not a part of the initial training data.

Machine learning techniques can be broadly classified into two main categories depending on whether the output values are required to be present in the training data. The first is "Unsupervised learning techniques" that require only the input feature values in the training data, and the provided learning algorithm discovers hidden structures in the training data based on just the input values. While the second form, the "Supervised learning techniques," requires the value of both the input and the output variable for each training sample to be known.[45]

Supervised Learning for Efficient ICFD

In supervised learning, each training sample comes in the form of a pair. The provided algorithm then trains a model that predicts the value of the output variables from the input variables using the defined features in the process. For supervised learning problems, we can quantify the performance of the trained model by measuring the difference between the known output values and the predicted ones. However, the error for this performance evaluation must not be measured on the training data but a separate test set. This ensures that the algorithm performance on novel data can be estimated correctly and gives an idea about the generalization of the learned model.[45]

Supervised machine learning creates a model that makes predictions based upon evidence in the case of uncertainty. A supervised learning algorithm uses a given set of input data and known outputs to those data and then trains a model to produce reasonable predictions for the output to new data.

Although ICFD plays a significant role in solving real-world flow systems, the burden of a heavy computation often compromises physical accuracy. Also, the process of ICFD analysis is based on imaging and other hemodynamic data and is often time-consuming due to the ample data process time, so its application has been majorly in preoperative assessment, planning, and predication rather than intra- or postoperative management. The surrogate flow model has the potential to attain both computational efficacy and physical precision. In principle, after training an accurate model, it can be employed to predict the outcomes for the interested fluid properties instantaneously. Therefore, time-consuming, complex ICFD simulations can be replaced by a surrogate model of ICFD, and physicians can have an informed decision regarding the patient's hemodynamics instantly. In this study, we used supervised learning to predict the velocity field for Hagen-Poiseuille and Womersley flows.

1.3 Research Objectives

In this work, we attempted to further develop our in-house ICFD solver *InVascular* in the following three aspects:

- To be able to work with diverse types of medical imaging data to perform 3-D anatomical extractions for ICFD.
- To perform several parametric studies with an idealized 3-D geometry for reliability and applicability of ICFD.
- Develop surrogate models to enable swift ICFD outcomes for both Hagen-Poiseuille and Womersley flows.

2. METHODOLOGY

For Image-based computational fluid dynamics (ICFD), the first step is image segmentation from patient-specific CT/MRI or SEM data. Several image processing, segmenting, and computational tools are used for that. Also, when we consider idealized geometries, they can be designed in CAD software packages. Once the 3-D flow domain is ready, then our in-house ICFD solver *InVascular* is incorporated to quantify the 4D velocity field. Finally, GPR machine learning techniques were explored to create surrogate models for predicting velocity with more computational efficiency within a 3D image-based pipe with renal arterial dimensions and flow conditions.

2.1 Image Segmentation

In our computational platform, *InVascular,* we start with segmenting medical image data in Standard Triangle Language (STL) data format and aim toward applying it not only to biomedical flows but also for parametric-designed flows in nature and engineering. Medical images from CTA or MRI are usually in DICOM format. Moreover, the images from SEM are usually in 8-bit/16-bit RGB format. Image segmentation is needed to extract the anatomical vessel before the vessel geometry is fed to the VLBM for hemodynamics. The raw DICOM and RGB images frequently include noises from various sources, and getting rid of these noises is always a crucial step in the image segmentation process to extract the anatomical vessels. Such a task usually varies from case to case with many uncertainties related to the imaging modality, disease conditions, machine resolution, scanning skills, etc. However, we have developed techniques for both DICOM image segmentation[46,47] and RGB image processing; we strongly recommend having rigorous image segmentation and processing with experience rather than simply running software with extensive manual inputs, as it affects the quantification of the hemodynamics.

All the modern CAD software packages, such as Siemens NX, and SolidWorks, can export their native files into STL format as well. The conversion from DICOM volumetric image to a 3-D vessel geometry in STL format[48] and construction of the 3-D vascular network from SEM image data is crucial as they directly affect the final flow domains for ICFD. Next sections, we will

describe the procedure to perform image segmentations from DICOM data, image processing, and 3-D construction from SEM data and create 3-D CAD models for idealized geometry assumptions.

2.1.1 DICOM Data

To quantify the ICFD in the human arterial system, we need the actual geometries of human arteries. For that, we will need patient-specific CT/MRI images. In this work, an open-source software package, 3D Slicer, was used for segmenting 3D geometries from these CT/MRI images.

3D Slicer[49] is an open-source software application for the visualization and analysis of medical image computing data sets. 3D Slicer can work with all generally used image data sets, such as images, segmentations, surfaces, annotations, transformations, etc., in 2D, 3D, and 4D. It supports multi-modality imaging, including CTA, MRI, and DUS. In this study, we used 3D slicer to segment the iliac artery, kidney, and connected artery and veins, vocal tracts to create the geometry for ICFD analysis. To perform segmentations in 3D Slicer, we used patient-specific DICOM data. Figure 1 shows a step-by-step process to create a segmentation of a kidney from patient-specific MRI data in 3D Slicer. This segmentation process can be divided into four significant steps:

Step 1: Image Acquisition and Data Loading

After collecting patient-specific DICOM data, the *Load DICOM Data* panel is used to import data to 3D Slicer. If collected patient data is in MATLAB data format, stacks of image slices are exported to 3D Slicer instead of using MATLAB for extraction. Once image data is imported into 3D Slicer, it arranges the image slices in three default slice views in which Axial, Sagittal, and Coronal slices of volume images can be displayed.

Step 2: Process Data and Segmentation

The segment editor module is used for segmentation. This module is for identifying the vessel of interest, or segments, in 2D/3D/4D images. This module contains several essential tools required to segment the geometry of interest. Some of the tools mimic a painting interface like photoshop or gimp but work on 3D arrays of voxels rather than on 2D pixels. The module can be

used for display in both 2D and 3D views, fine-grained visualization options, editing on slices in any orientation, editing in 3D views, editing of overlapping segments, creating segmentation by interpolating or extrapolating segmentation on a few slices. First, the *Paint* tool is used to highlight and specify an approximate region of interest. Next, the *Threshold* tool is used to define a threshold range and save outputs to a selected segment, or we can use it as an editable intensity range for creating vessel segmentations.

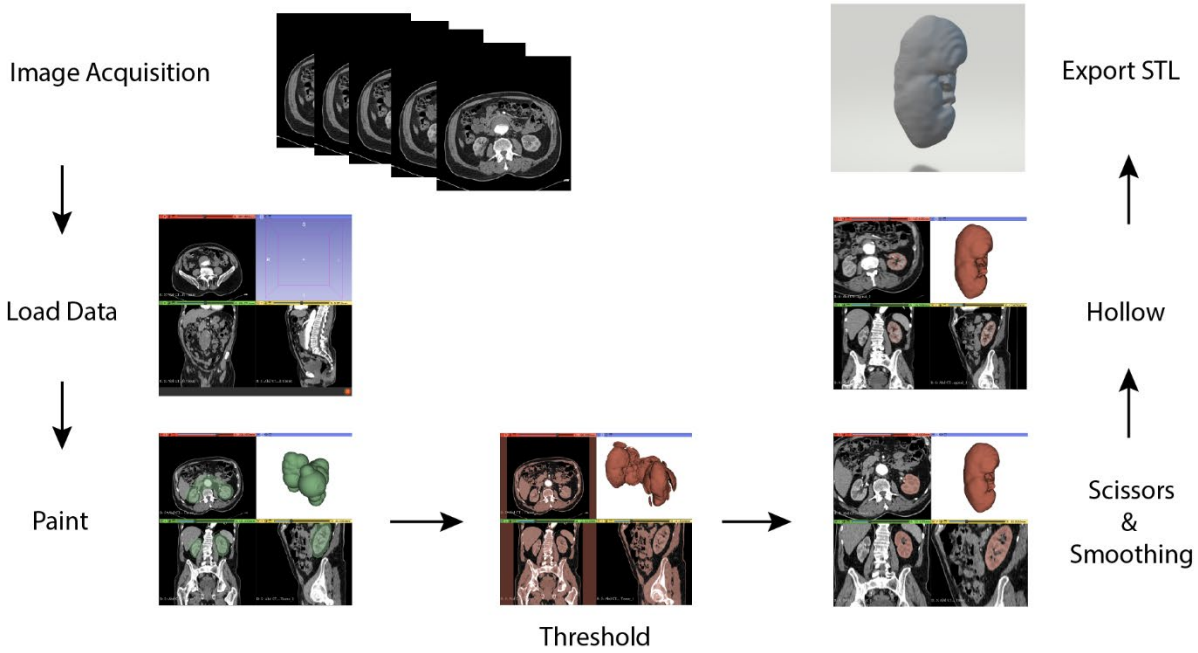

Figure 1. Steps of kidney segmentation in 3D Slicer

Step 3: Refining Segmentation

After thresholding, the geometries are usually very uneven and contain many broken parts due to pixelated image data. Therefore, the *Scissor* tool is used to cut off all the extra parts, and then the *Smoothing* tool is used for filling in holes and removing extrusions.

Step 4: Hollowing and Exporting

Once satisfied with the geometry, it is then made hollow using the *Hollow* tool by replacing the segment with a uniform-thickness shell defined by the segment boundary. Finally, using the *Export* section of the *Segmentations* module, the created segment is exported as an STL file for processing in our in-house computational modality *InVascular*.

2.1.2 SEM Data

In this work, SEM data was collected for the choroid, also known as the choroid coat or choriocapillaris. It is a part of the vascular layer that is located between the retina and the sclera of the eye. Its primary function is to provide nutrients for the retina and glass body and to provide a darkroom environment for the entire eye so that the reflected image is clear.

To construct the 3D model of the choroid layer, we used raw patient-specific SEM image data in both 8-bit/16-bit RGB formats. Figure 2 and 3 shows step-by-step process to create a 3D model of the choroid layer from patient-specific SEM image data. This modeling process can be divided into two major steps:

Step 1: Image Processing

After collecting patient-specific SEM image data in RGB format, MATLAB is used for image processing. First, MATLAB is used to convert the raw image (8-bit/16-bit RGB format) into an 8-bit Grayscale image. Then a threshold value is assigned to convert the 8-bit intensities of each pixel of the Grayscale image into binary to convert it into a binary image. Next, the Binary image is refined by performing a few morphological operations using MATLAB image processing tools.

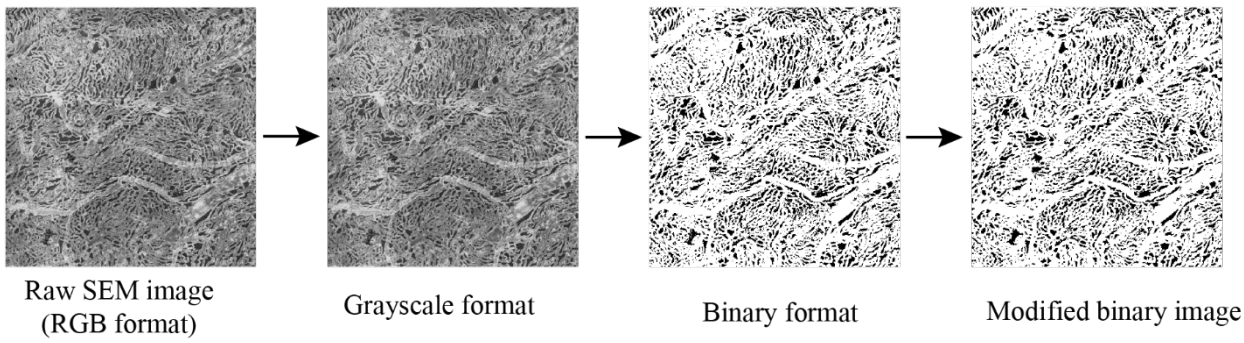

Figure 2. Steps of image processing for Choroid

Step 2: Erosion And 3D Model Construction

Next, the arterioles and venules are identified for the same patient-specific image data. Then a smaller portion of the exact location of both the refined binary image and the arteriole-venule image is cropped. Next, the cropped binary image is eroded to create a series of images,

and MATLAB is used to create a 3D geometry connecting these eroded image layers to the arteriole venule image layers. Thus, the 3D geometry of the choriocapillaris is constructed.

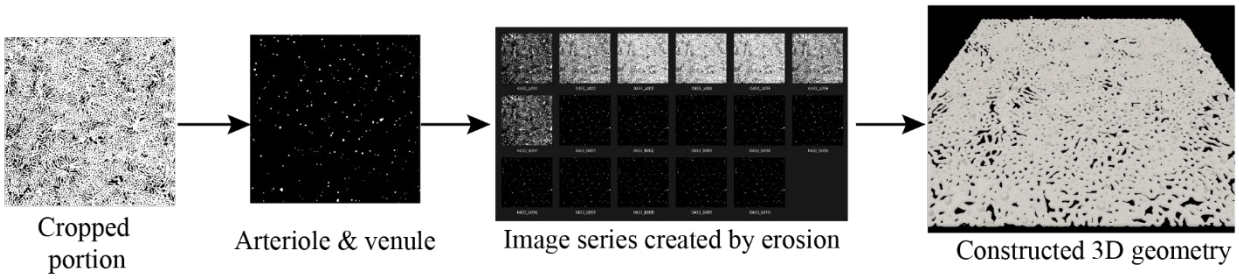

Figure 3. Steps of 3-D construction of choriocapillaris

Once the 3-D geometry is derived, VLBM can be used to derive the hemodynamics inside the vascular layer, but that is beyond the scope of this study.

2.1.3 CAD Data

To reduce the computational cost for ICFD simulations of complex and arbitrarily shaped arteries, idealized geometries can be considered to perform validation and parametric study. In this work, we assumed a 3-D pipe as the straight portion of the human renal artery and used it for conducting a parametric study using our in-house ICFD solver, *InVascular*. We also created stenosis inside the pipe to explore the effects of stenosis severity on RI. We also created several other idealized geometries to simulate curved and bifurcated arteries. The idealized geometries were generated in commercial software packages Siemens NX and SolidWorks.

Siemens NX:

We used Siemens NX to design and create a 3-D pipe with renal arterial dimensions with no stenosis as well as with various severities of stenosis. For our computational analysis in VLBM method, we designed the pipe as such it is enclosed inside a 3D elongated cube or cuboid to differentiate between the flow domain inside and outside the pipe.

3D Pipe with No Stenosis

Figure 4 shows the step-by-step process of creating an image-based 3D pipe with no stenosis inside it in Siemens NX.

Step 1: Sketch Profile

First, a sketch plane is selected. In this case, the top plane is selected as the sketch plane. Next, a circle and a square profile are sketched. Finally, appropriate dimensions are given to the circle and the square based on renal arterial dimensions.

Step 2: Extrude and Subtract

After completing the sketch, the extrude tool is used to extrude the square to create a cuboid. Next, the Extrude tool is used again to extrude the circle to create a cylinder and subtract it from the cuboid. The dimensions for the cylinder and the cuboid are given as such; the cylinder is entirely enclosed by the cuboid. This enclosed cylinder has the diameter of the average inner diameter of a renal artery in humans.

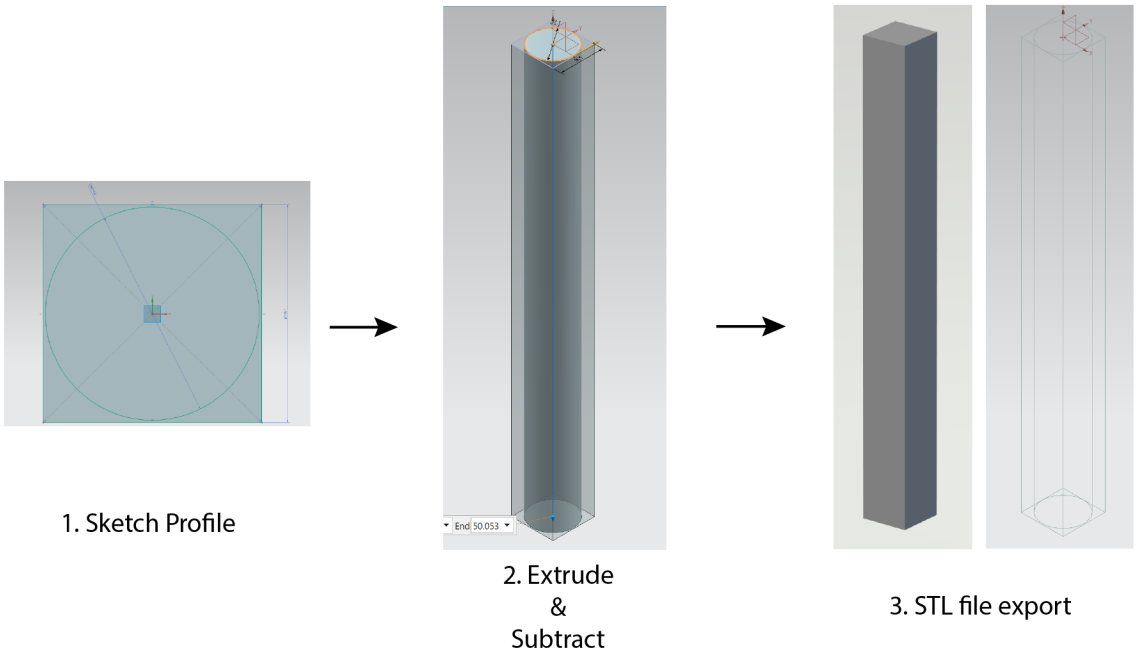

Figure 4. Design steps for a 3D pipe with no stenosis in Siemens NX

Step 3: STL File Export

Finally, the created geometry is exported in STL format for the CFD analysis. In Figure 4 the wireframe picture shows the enclosed cylinder within the cuboid.

3D Pipe with Stenosis

Creating stenosis inside CAD software can be extremely complicated, as the shape of the stenosis can be very arbitrary. In this work, the Spline tool in Siemens NX was used to ensure the natural curves and bends of stenosis. Figure 5 shows the step-by-step process of creating stenosis in Siemens NX.

Step 1: Sketch Stenosis

Smoothing and Hollow. First, a sketch plane is selected. In this case, the front plane is selected as the sketch plane. Next, the side profile of the stenosis is sketched using the spline tool. Different severity of stenosis can be created by giving different heights and surface areas to this sketch of stenosis.

Step 2: Fill Surface and Revolve

After completing the sketch, the Fill surface tool is used to fill the stenosis surface. Next, the Revolve tool is used to revolve the surface at 200° to create the 3D stenosis geometry.

Step 3: Sketch Profile

Like the previous no stenosis case, the top plane is selected as the sketch plane. Next, a circle and a square profile are sketched. Finally, appropriate dimensions are given to the circle and the square based on renal arterial dimensions.

Step 4: Extrude

Like the previous no stenosis case, the Extrude tool is used, but instead of extruding the square, the region between the square and the circle is extruded to create the subtraction of the cylinder from the cuboid. The dimensions for the cylinder and the cuboid are given as such; the

cylinder is enclosed within the cuboid. Nevertheless, this time, it is open on the top and the bottom. The cylinder still has the diameter of the average inner diameter of a renal artery in a human.

Step 5: Trim and Delete Body

Next, the intersected volumes of the 3D stenosis and the pipe wall are subtracted from this 3D pipe, and the remaining 3D stenosis and pipe are united to create a single 3D geometry.

Step 6: Unite and Edge Blend

Smoothing and Hollow. Next, the edge of the 3D stenosis is blended to create a uniform surface inside the 3D pipe, just like naturally occurring stenosis in renal arteries.

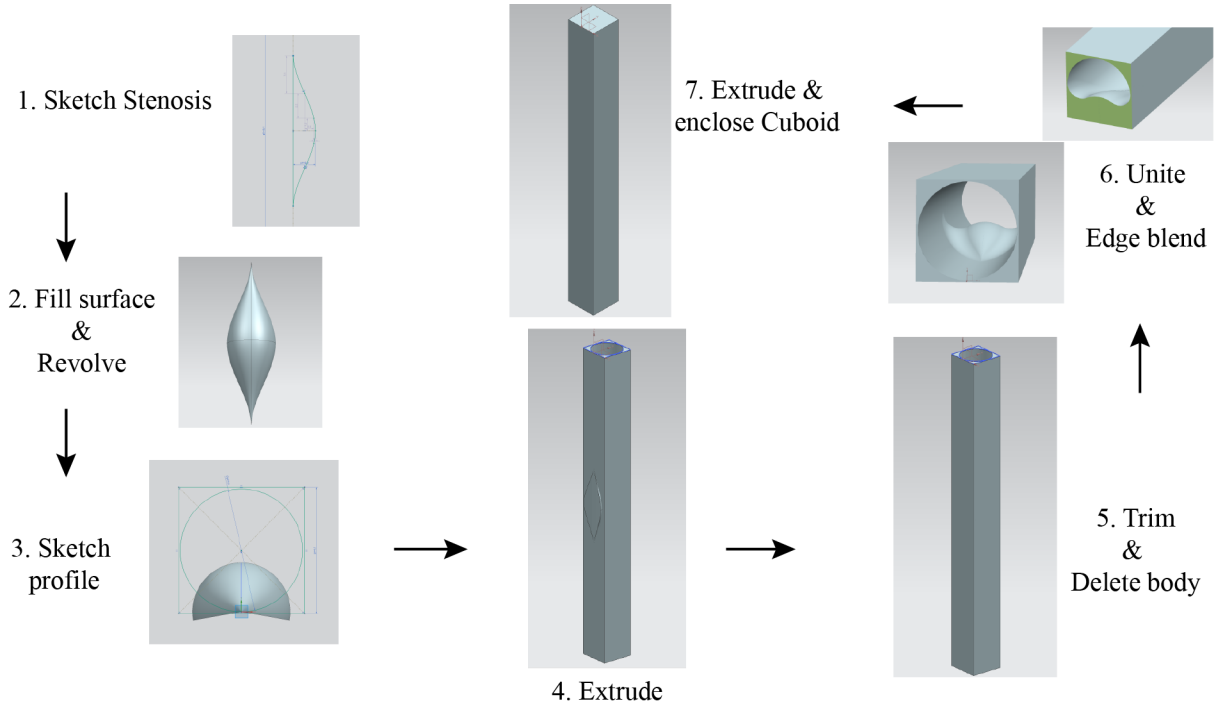

Figure 5. Design steps for a 3D pipe with stenosis in Siemens NX

Step 7: Extrude and Enclose Cuboid

Finally, the square sketch created in step 3 is extruded to enclose the top and bottom surfaces of the 3D pipe to create the enclosed 3D pipe geometry with stenosis.

SolidWorks

We used SolidWorks to design the idealized curved aorta and bifurcated artery. We created the inner volume of the geometries. Figure 6 shows the step-by-step process of creating an idealized curved aorta and bifurcated coronary artery in SolidWorks. The entire process could be divided into four significant steps. Although for creating an idealized curved aorta, Revolve step is not needed.

Step 1: Sketch

First, the profile of the 3D geometry was sketched on a plane. For the Curved aorta, it was the path to Sweeping. Furthermore, for a bifurcated artery, we create a rectangle to create the single-arm with Revolve tool.

Step 2: Revolve

Curved aorta design does not require this step. However, for the bifurcated artery, the rectangle created don the previous step was revolved 360° to complete the single cylindrical arm. Next, one of the bifurcated arms is sketched from the bifurcation.

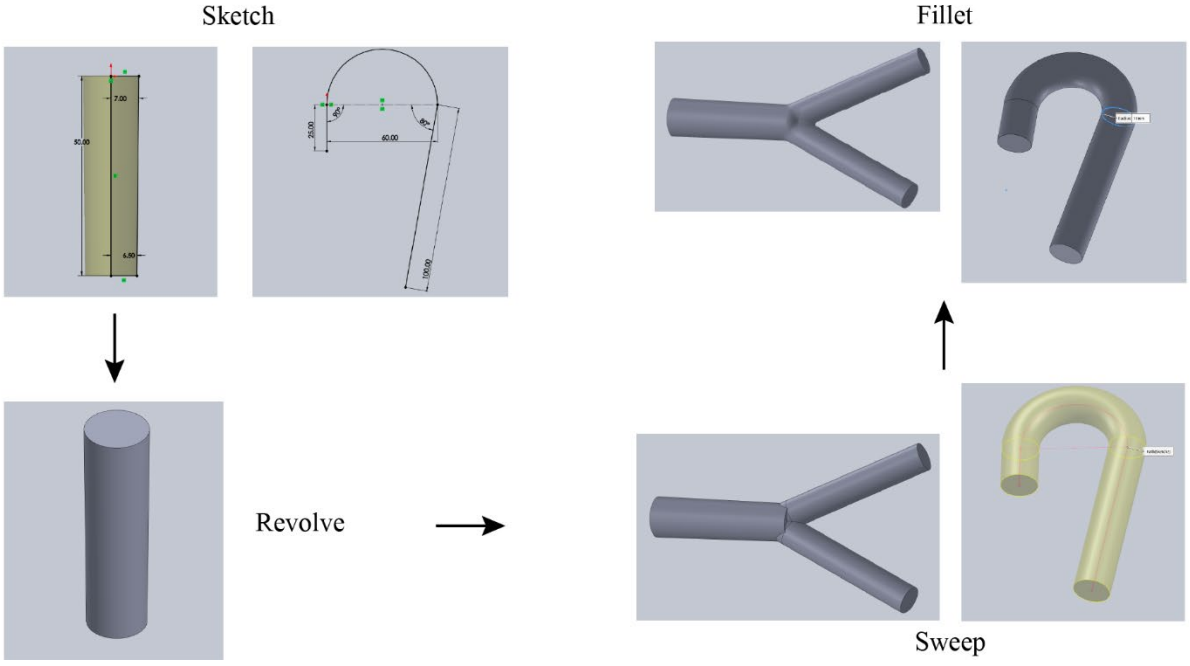

Figure 6. Design steps for curved and bifurcated pipes in SolidWorks

Step 3: Sweep

For the Curved aorta, a circular profile is swept throughout the sketch drawn in step 1. For the bifurcated artery, a circular profile is also swept along the bifurcated arm. Next, it is mirrored to create the second bifurcating arm.

Step 4: Fillet

Finally, the fillet tool is used to smooth out any sharp edges and corners. Once completed, the 3D geometry can be exported in STL format for further CFD analysis.

2.2 Computational Fluid Dynamics of Pulsatile flows in Pipes

In this work, we used a unique computational platform for quantifying the 4-D velocity field in image-based pulsatile flows using the volumetric lattice Boltzmann method (VLBM).[42] The novelty of this computational approach consists of (1) a unique extraction of flow domain from image data, (2) a seamless connection between the output of image processing and the input of CFD, and (3) GPU parallel computing processing[41,44,50,51] to significantly mitigate the computation burden. To simulate a broad class of complex flows, including pore-scale porous media flow, [52-56] multiphase/multicomponent flows[1,43,57-59] the kinetic-based lattice Boltzmann modeling has emerged. The main advantages related to this work are its amenability for modeling the intermolecular interactions at the two-phase interface to recover the appropriate multiphase dynamics without demanding computing cost and its suitability for scalable GPU (Graphics Processing Unit) parallelization[41,44,51,57,60-65] to achieve fast computation.

The VLBM was developed explicitly for complex flows in arbitrary and willfully moving boundaries,[42] in which the fluid particles are uniformly distributed in lattice cells, as opposed to sitting at lattice nodes in conventional LBM. As schematized in Figure 7, an arbitrary boundary (black line) separated a fluid domain (without dots) from a solid boundary structure (with dots).

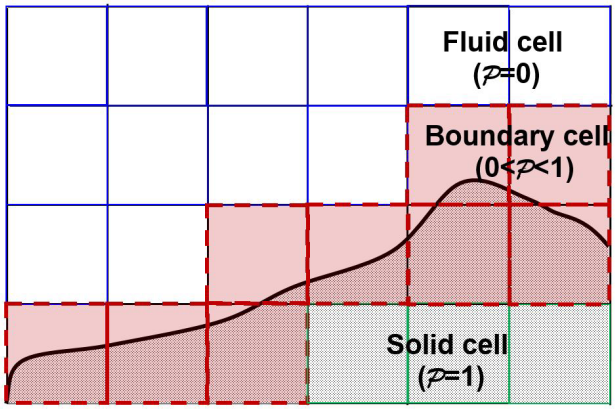

Figure 7. Schematic of cell-based space in VLBM distinguishing types of lattice cells: fluid cell (P = 0), solid cells (P = 1), and boundary cell (O < P < 1). The solid line represents an arbitrary boundary of the ow domain

Three distinct cells are characterized through the occupation of solid volume $\Delta V_s(x)$in the cell with a total volume $\Delta V(x)$, defined as $P(x) \equiv \Delta V_s(x)/\Delta V(x)$.Thus, three different cells, fluid cell ($P = 0$), solid cell ($P = 1$), and boundary cell ($0 < P < 1$), can be distinguished through the value of P. The detailed formulation of LBM for CFD is referred to in our group's previous publication[41]. The VLBM equation deals with the time evolution of the particle population, $n_i(x,t)$, corresponding to the i-th velocity for $i = 0, \dots, b$:

$$n_i(x + e_i\delta t, t + \delta t) = n_i(x,t) - \left[n_i(x,t) - n_i^{eq}(x,t)\right]/\tau \tag{2.1}$$

$$n_i^{eq}(x,t) = N\omega_i\left[1 + \frac{e_i \cdot u}{c_s^2} + \frac{(e_i \cdot u)^2}{2c_s^4} - \frac{u \cdot u}{2c_s^2}\right] \tag{2.2}$$

with ω_i is an appropriate weight of the i-th velocity direction, c_s is the speed of sound, $N(x,t)\left(= \sum n_i(x,t)\right)$ and $N(x,t)u(x,t)\left(= \sum e_i n_i(x,t)\right)$ are the total particle population and particle momentum in the cell, respectively.

To depict the streaming part, we rewrite the right-hand side of equation (2.1) as

$$n_i'(x,t) = n_i(x,t) - \left[n_i(x,t) - n_i^{eq}(x,t)\right]/\tau \tag{2.3}$$

Where $n_i'(x,t)$ represents the "post-collision" particle population. Due to the existence of boundary cells, there would be only an appropriate volume fraction of fluid particles streaming to its neighboring cell. After a streaming operation, particles in cell x at time $t + \Delta t$ are from two sources: (i) streaming from its upwind neighboring cells, $[1 - P(x,t)]n_i'(x - e_i\Delta t, t)$, and (ii) bounce-back from the downwind cells $P(x + e_{i^*}\Delta t, t)n_{i^*}'(x,t)$, as shown below.

$$n_i''(x, t + \Delta t) = [1 - P(x,t)]n_i'(x - e_i\Delta t, t) + P(x + e_{i^*}\Delta t, t)n_{i^*}'(x,t) \tag{2.4}$$

Where i^* corresponds to the direction opposite to the i-th direction $e_{i^*} = -e_i$. This modified streaming process makes sure that particles are reflected in their appropriate locations in the fluid domain but does not introduce any extra mass. For the current research, we focus on the integration of inlet/outlet BCs with VLBM. The entire computational platform is called InVascular.[66-68] *InVascular* starts with feeding the $P(x)$ of each cell to VLBM[42] (with D3Q19 lattice model), together with the inlet/outlet boundary conditions, for ICFD.

The resulting density, velocity, and pressure are obtained as $\rho(x,t) = \sum n_i(x,t)/[1 - P(x,t)]$ and $u(x,t) = \sum e_i n_i(x,t)/\sum n_i(x,t)$. In LBM, including node-based and cell-based representation, the relationship between density and pressure is

$$p(x,t) - p_0 = c_s^2[\rho(x,t) - \rho_0] \tag{2.5}$$

For inlet and outlet BCs, we employ the non-equilibrium extrapolation boundary condition as follows

$$n_i(x_b,t) - n_i^{eq}(x_b,t) = n_i(x_f,t) - n_i^{eq}(x_f,t) \tag{2.6}$$

for i-th direction where x_b and x_f are the boundary cell and the fluid cell next to the boundary cell in the i-th direction. If velocity is known at the boundary $u(x_b,t)$ cell, the velocity BC is

$$n_i(x_b,t) = n_i^{eq}\left(\rho(x_f,t)u(x_b,t)\right) + n_i(x_f,t) - n_i^{eq}(x_f,t) \tag{2.7}$$

whereas if pressure $p(x_b,t)$ is given, the pressure BC reads

$$n_i(x_b,t) = n_i^{eq}\left(\rho(x_b,t)u(x_f,t)\right) + n_i(x_f,t) - n_i^{eq}(x_f,t) \tag{2.8}$$

where $\rho(x_b,t)$ is calculated from equation 2.5. The outstanding advantage of *InVascular* is its revolutionary fast computational speed realized by the innovative GPU parallel computing technology; thus, *InVascular* is ideal for clinically oriented applications.

2.2.1 Design Geometry

The 3D geometries for ICFD analysis are constructed in CAD software packages like Siemens NX, SolidWorks, etc. For the parametric study, the geometries with varying stenosis severity were also created. A parameter was used to determine the severity of stenosis.

Stenosis Severity,

$$\text{Diameter reduction, } S_D = \frac{Dia\ with\ Stenosis}{Dia\ without\ Stenosis} = \frac{D_S}{D_0}$$

$$\text{Volume reduction, } S_V = \frac{Volume\ with\ Stenosis}{Volume\ without\ Stenosis} = \frac{V_S}{V_0}$$

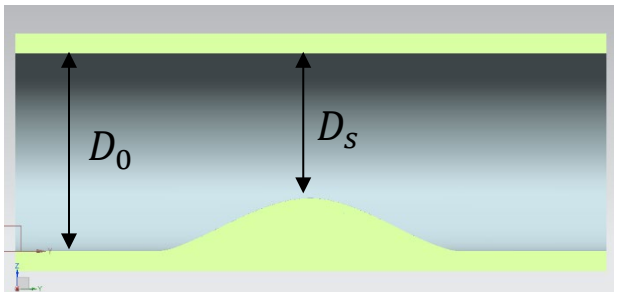

Figure 8. Schematic for Stenosis severity parameter

For this study, five different 3-D pipe geometries were created in Siemens NX to simulate the stenosis severity based on diameter, S_D at 0%, 20%, 40%, 60%, and 80%. The sectional images for all these geometries are shown below in Figure 9.

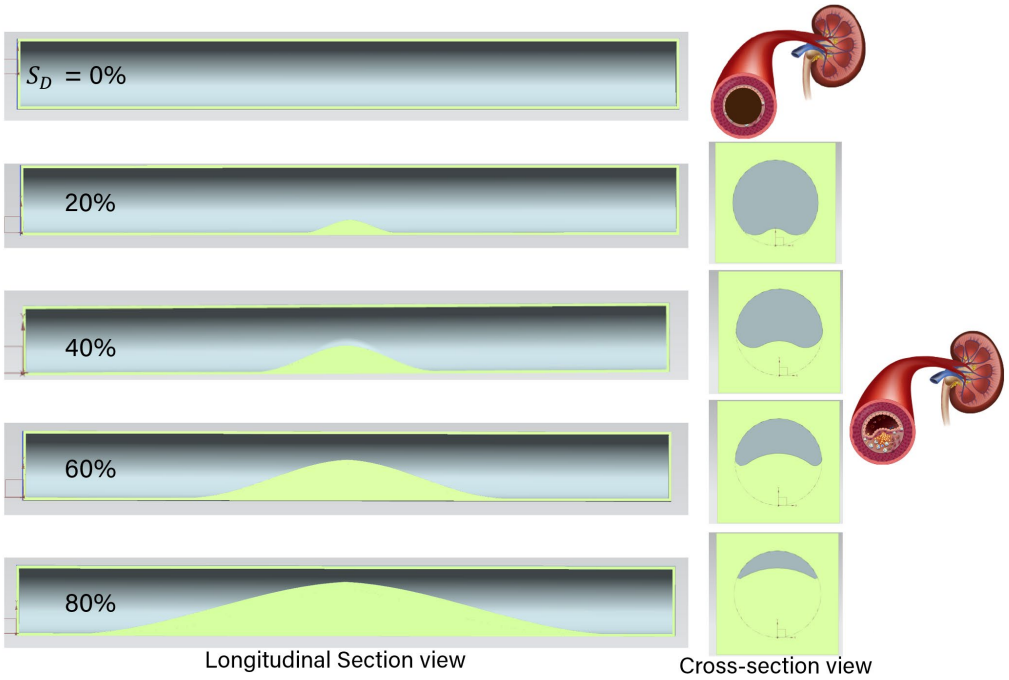

Figure 9. Sectional views of pipes with varying stenosis severity

2.2.2 Boundary Conditions

In patient-specific ICFD, the vessel wall is considered static and rigid. The boundary conditions include a no-slip condition on the vessel walls and a pulsatile velocity condition based on DUS evaluation at the inlet and outlet. The pulsatile flow along the pipe in the z-direction was driven by a pressure gradient. A no-slip boundary condition is considered on the pipe wall, realized by the bounce-back boundary condition. The initial conditions are constant pressure and parabolic

velocity in the entire flow domain. In this study, the fluid was considered human blood, and it was assumed as a Newtonian fluid having a density of $1025\ kg/m^3$ and kinematic viscosity of $3.415 \times 10^{-6} m^2/s$ was assumed.

2.2.3 Post-processing

After the simulation was run on a computer capable of GPU parallel computing, the output was derived as a 4-D velocity field of all the cells inside the 3-D pipe. MATLAB and Tecplot were used for post-processing the 4D velocity field data. For post-processing, velocities were calculated at specific locations inside the 3-D pipe geometry at specific time points. Also, to conduct the parametric study, pulsatile parameters heart rate and pulsatile pressure gradient were varied, and for each case, velocities at specified locations and time points were calculated to derive RI. Finally, the change of RI based on the change of pulsatile parameters and severity of stenosis were documented.

2.2.4 Validation

A relative error convergence check was done to find the optimum spatial resolution for the ICFD analysis. Next, the ICFD results for the optimum resolution case were verified against the analytical solution of the Womersley equation. Normalized velocity vs. normalized radius results was derived for a specific location and specific time-stamps for both ICFD and analytical solution, and a comparison between the two was conducted for the validation of the ICFD process. Also, the results for the effects of pulsatile parameters on RI were compared with experimental results.

2.3 Surrogate Modeling

Gaussian processes (GPs) are natural generalizations of multivariate Gaussian random variables to infinite index sets. GPs have been employed in many disciplines to a diverse range of ends. Gaussian process regression (GPR) models are probabilistic models based on a nonparametric kernel. In this work, we developed a numerical procedure using Gaussian Process Regression (GPR) to show the potential of machine learning methods in constructing efficient and precise surrogate models for Hagen-Poiseuille and Womersley flows that include spatial and spatial-tempo responses, respectively.

A MATLAB toolbox for working with kriging approximations to computer models, Design and Analysis of Computer Experiments (DACE),[69] was used for creating the GPR models in this work. Typical usage of this software is to build a kriging approximation model based on data from a computer experiment and use this approximation model as a surrogate for the computer model or analytical equation results. A computer experiment here is a collection of pairs of input and outputs from runs of a computer model or original flow model in this case. Both the input and the outputs from the computer model can be high dimensional. In this study, we implement machine learning methods to make predictions for speedy ICFD results.

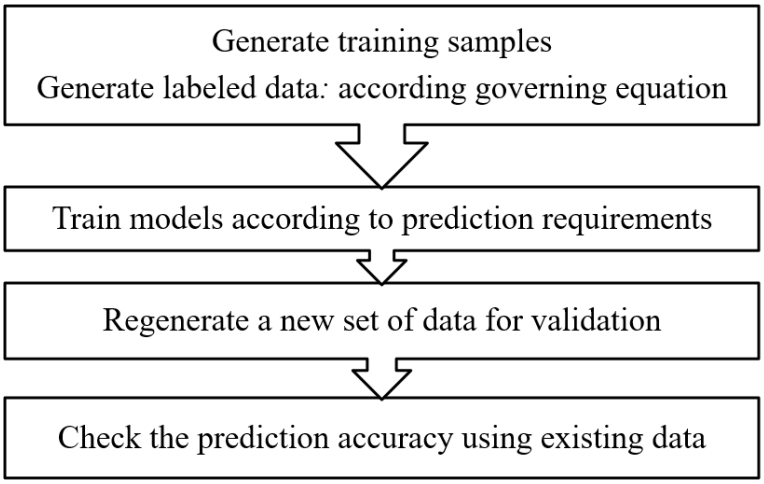

Figure 10. Flow chart of model development in Gaussian Process Regression

We used limited runs of the original flow models and applied them to generate the training data by calling the analytical solutions multiple times with evenly discretized spatial or spatial-temporal variables. We compared the GPR method with several other ML methods and explored the unique feature of the DACE model. Moreover, to check the accuracy of the surrogate model predictions, the predicted results were compared with both ICFD and analytical results.

2.3.1 Hagen-Poiseuille Flow

In fluid dynamics, the Hagen–Poiseuille equation, is a physical law that gives the pressure drop in an incompressible and Newtonian fluid in laminar flow flowing through a long cylindrical pipe of a constant cross-section. The analytical solution for the Hagen–Poiseuille flow is given below:

$$\text{or, } u_r = \frac{u_{max}}{R^2}(R^2 - r^2) \tag{2.9}$$

This equation was used to create the training dataset with r, R, u_{max} as inputs and u as outputs. Next, a surrogate model was created based on the DACE model of the GPR method, and the predictions from the trained model were evaluated using a new test dataset generated using the same equation 2.9. Once the surrogate model predictions reached an acceptable margin of error, the results were compared against both ICFD and analytical results.

2.3.2 Womersley Flow

Pulsatile flow or Womersley flow is a flow with periodic variations. Pulsatile flows can be easily found in a wide range of engineering and scientific systems. Examples include pulmonary ventilating[70,71] and blood circulating[72] in biological flows, sediment transport in coastal flows[73], and reciprocating flow in internal combustion engines[74]. The flow profiles were first derived by John R. Womersley (1907–1958) in his work with blood flow in arteries.[75] The analytical solution for the Womersley flow is as follows:

$$\frac{u}{u_{max}} = \left(1 - \frac{r^2}{R^2}\right) + \frac{4A}{\alpha^2} Real\left\{\frac{1}{i}\left[1 - \frac{J_0\left(\frac{\alpha r}{R} i^{\frac{3}{2}}\right)}{J_0\left(\alpha i^{\frac{3}{2}}\right)}\right] e^{i\omega t}\right\} \tag{2.10}$$

This equation was used to create the training dataset with r, R, u_{max}, A, and α as inputs and velocity u as outputs. Next, a surrogate model was created based on the DACE model of the GPR method, and the predictions from the trained model were assessed using a new test dataset generated using the same equation 2.10. Once the surrogate model predictions reached a negligible range of error, the results were compared against both ICFD and analytical results.

3. APPLICATIONS

We first demonstrate the image segmentation and generation of 3D STL files from patient-specific DICOM data for different human arteries and organs. Next, we do a 3-D construction of choriocapillaris from SEM data. Then, we create idealized arteries in CAD software packages. Next, we use one of the idealized arterial geometries, a 3-D pipe, to quantify the 4D velocity field using *InVascular* and validate it against the analytical solution of Womersley flow. Finally, we implement supervised machine learning methods to create surrogate models to predict ICFD results for the idealized image-based pipe geometry for both Hagen–Poiseuille and Womersley flow and compare the predictions against both ICFD results and analytical solutions.

3.1 Image Segmentation

We first demonstrate the image segmentation and generation of 3-D STL files from patient-specific DICOM data using the open-source software package 3D Slicer. We created image segmentations of human kidneys and connected aortorenal arteries and veins from patient-specific MRI image data. We also segmented the iliac artery from CTA images.

Kidneys and Aorto-renal Arteries and Veins

We used 3D slicer and segmented both kidneys along with their connecting renal arteries and veins and aorta using patient-specific DICOM data. Figure 11(a) shows the 3D segmented geometry, including both left and right kidneys and connected renal artery, vein, and aortas from the 3D slicer final STL file. Figure 11(b) shows the 3D segmented geometry, including the left kidney and connected renal artery and vein from 3D slicer final STL file.

The image segmentation process was incredibly challenging. As the CTA data included noise and the resolution was not remarkably high as well, segmenting the smaller arteries and veins manually was a very demanding task. Moreover, when hollowing these tiny arteries and veins, we had to go through slice by slice through the images to ensure the flow path was not blocked or partially blocked. Finally, ensuring that the arteries and veins are connected to the kidneys was also challenging. To confirm that, we checked the cross-sectional views of the connection regions.

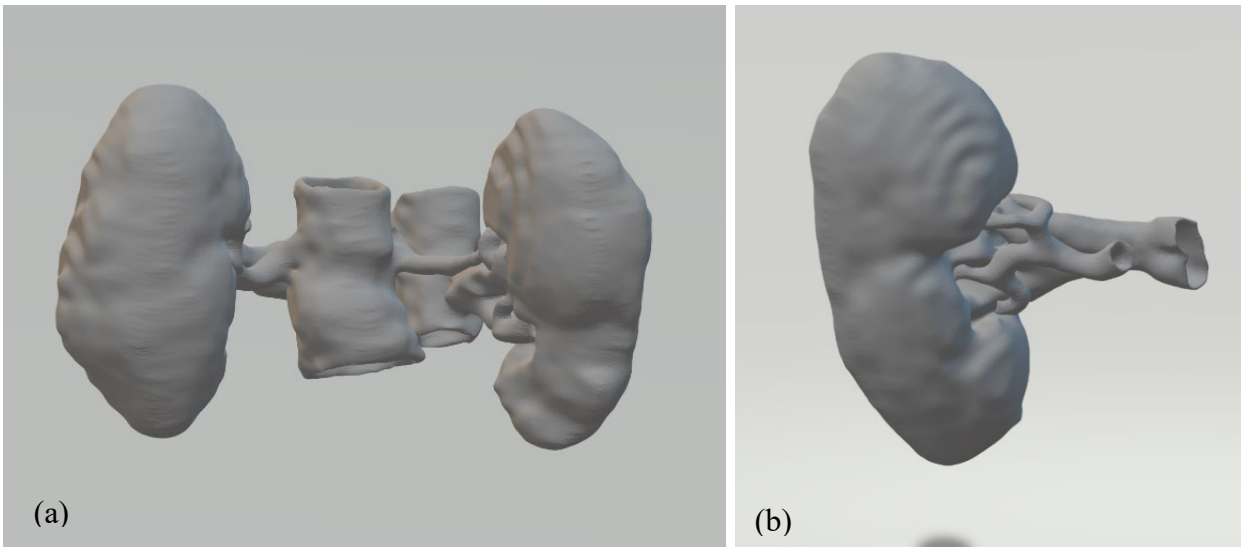

Figure 11. (a) 3D view of the segmentation of both kidneys with connected aortorenal arteries, veins, and aortas (b) 3d view of a single kidney with its connected artery and veins

The geometry was initially segmented as solid and afterward was made hollow using the *Hollow* tool from 3D Slicer.

Iliac Artery

We also used 3D slicer to segment the bifurcated iliac artery using patient-specific CTA data. Figure 12 shows the 3D segmented geometry.

Figure 12. 3D view of iliac artery segmentation

For this particular case, the segmentation in the bifurcation region was really intricate. Due to the low pixelated resolution, determining the lumen edge was difficult. So, several adjustments to the brightness and contrast of the CTA images were made to make the image slices clearer and the edges more visible.

Vocal Tract

We also segmented vocal tract geometry from MRI images and MATLAB data. We used MATLAB, commercial programming, and a numeric computing platform for extracting MRI data for 3D Slicer. Patient data were collected from USC Speech and Vocal Tract Morphology MRI Database.[76] MATLAB was used to extract image sequences from the data files, and then 3D Slicer was implemented for segmentation. Here the 3D volumetric MRI scan of a female patient vocalizing the vowel "bought" was used as image data.

Figure 13. 3-D vocal tract segmentation from 3D Slicer

After the segmentation, the *Hollow* tool was used to make the vocal tract hollow, and the *Scissor* tool was used to create inlet and outlet openings. For this case, having anatomical knowledge of the vocal tract was crucial. Understanding where the vocal tract is located in the three 2-D views of MRI images and distinguishing between the nasal passage and the vocal tract was also important. Moreover, the MRI data was of exceptionally low resolution, and in many image slices, the vocal tract lumen is shown as broken with isolated pixels. Connecting those isolated portions manually on the right path was very intricate and laborious.

3.1.1 SEM Data

To construct the 3D model of the choroid layer, we used raw patient-specific SEM image data in RGB format, and the MATLAB image processing toolbox was implemented for further image processing. First, the RGB image is processed into a Binary image. Then a cropped portion of the image is eroded into an image series based on the arteriole and venule connection image in MATLAB. Finally, the image slices are connected to construct the 3-D geometry of the choriocapillaris layer. Figure 14 shows the cropped binary image and the top view of the 3-D geometry, and the 3-D view of the vascular layer.

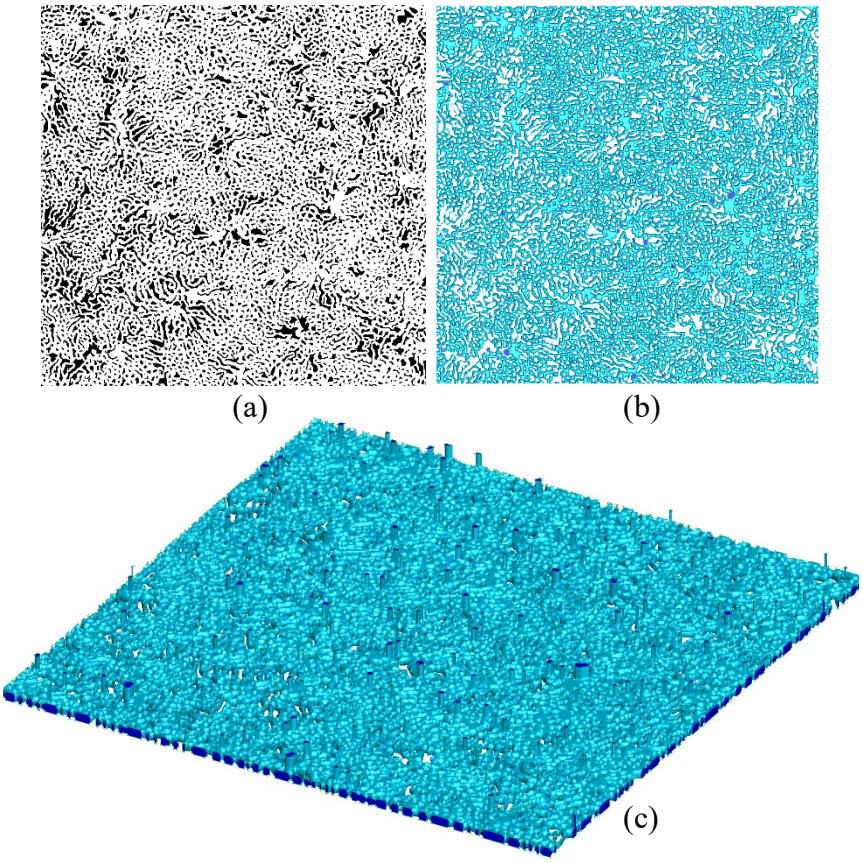

Figure 14. (a) Cropped binary image, (b) 3-D choriocapillaris geometry top-view, (c) 3-D choriocapillaris geometry isometric-view

We also segmented the choriocapillaris layer for two other cases from patient-specific SEM data and constructed a 3-D flow domain.

3.1.2 CAD Data

In this work, for ICFD analysis and parametric study, we used idealized geometries. We created a 3-D pipe geometry simulating the straight portion of an idealized renal artery using the commercial CAD software package Siemens NX. We also created pipes with varying stenosis severity for the parametric study in Siemens NX. Finally, we created an idealized curved aorta and a bifurcated coronary artery in SolidWorks.

Idealized Renal Artery

The straight section of a renal artery can be assumed as a straight pipe with similar diameter and length. Therefore, we used Siemens NX to design the pipe geometry with renal arterial dimensions.

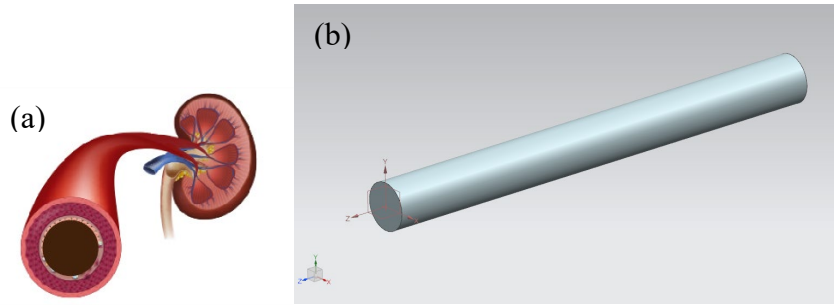

Figure 15. (a) A renal artery with no stenosis, (b) Inside volume of the 3-D pipe geometry with no stenosis

We also created stenosed pipe geometries in Siemens NX. Pipes with varying stenosis severity were created for parametric study. Figure 16 shows a diseased renal artery with stenosis and the cross-section of a pipe geometry with similar stenosis inside it.

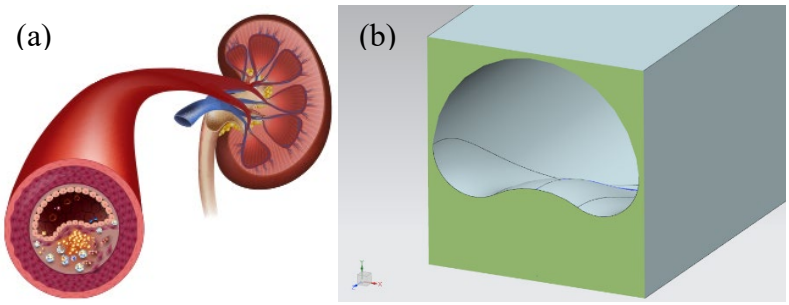

Figure 16. (a) A renal artery with a stenosis, (b) Cross-sectional view of the pipe geometry with stenosis

Four different stenosis severity pipe geometries were created for the parametric study. In all the cases, Sd and Sv were calculated afterward.

Idealized Curved Aorta

SolidWorks, a commercial software package, was used to design an idealized curved aorta with similar diameters and curvatures. The radius of curvature and the length of the larger arm of the aorta were varied to create several design variations to conduct a parametric study to find the effect of these parameters on the flow field inside the aorta.

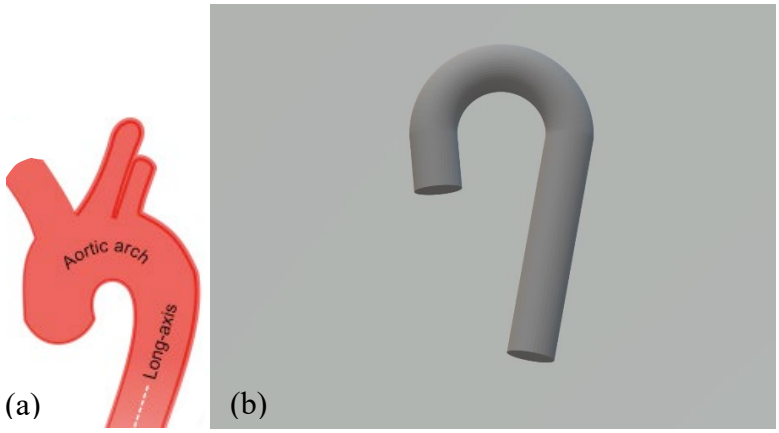

Figure 17. (a) A typical curved aorta, (b) Fluid volume inside the designed curved pipe

For the parametric study, one parameter was changed at a time, keeping all other parameters unchanged.

Idealized Bifurcated Coronary Artery

SolidWorks, a commercial software package, was used to design an idealized version of a bifurcated coronary artery with a similar diameter and angle of bifurcation. The diameters of the arteries and the angle of bifurcation were varied to create several design variations to conduct a parametric study to find the effect of these parameters on the flow field inside the artery.

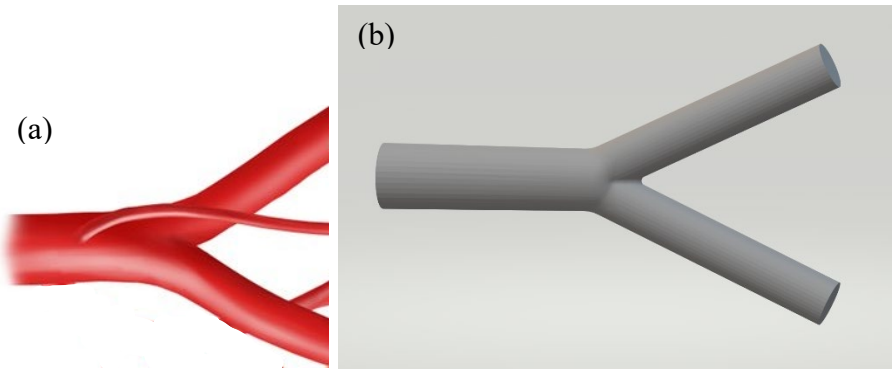

Figure 18. (a) A typical bifurcated artery, (b) Fluid volume inside the designed bifurcated pipe

For the parametric study, one parameter was changed at a time, keeping all other parameters unchanged.

3.2 Parametric Study

We conducted two studies to demonstrate the reliability and applicability of our computational method. The first one is a parametric study of pulsatile flows in an image-based 3D pipe with no stenosis. We simulated Womersley (laminar) flows and compared the 4-D computed fields of the velocity with analytical solutions. The second one quantifies 4-D fluid dynamics in the image-based 3D pipe with varying severities of stenosis and their corresponding RI.

3.2.1 Computational Setup

A 3-D rigid, right-circular straight pipe generated in Siemens NX in STL format with a length L = 50 mm and a radius R = 2.5 mm. The pulsatile flow along the pipe in the z-direction was driven by a pressure gradient. A no-slip boundary condition is considered on the pipe wall, realized by the bounce-back boundary condition. The initial conditions are constant pressure and parabolic velocity in the entire flow domain. A uniform mesh in the VLBM is used with the cell number, N_D across the pipe diameter to represent the spatial resolution. The volumetric parameter $P(x)$ of each lattice cell is calculated based on the STL file by our in-house MATLAB code.

Flow is driven by a pressure gradient,

$$\frac{\partial P}{\partial L} = P_s + P_0 * e^{i\omega t}$$

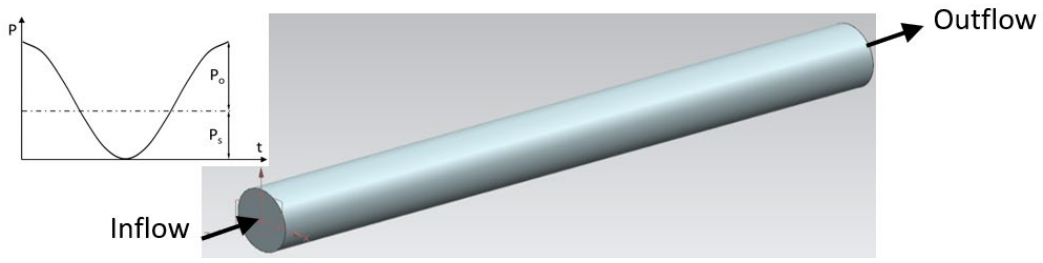

Figure 19. Flow domain and computational setup

Here, P_s = Mean pressure gradient

P_0 = Fluctuation of pulsatile pressure gradient

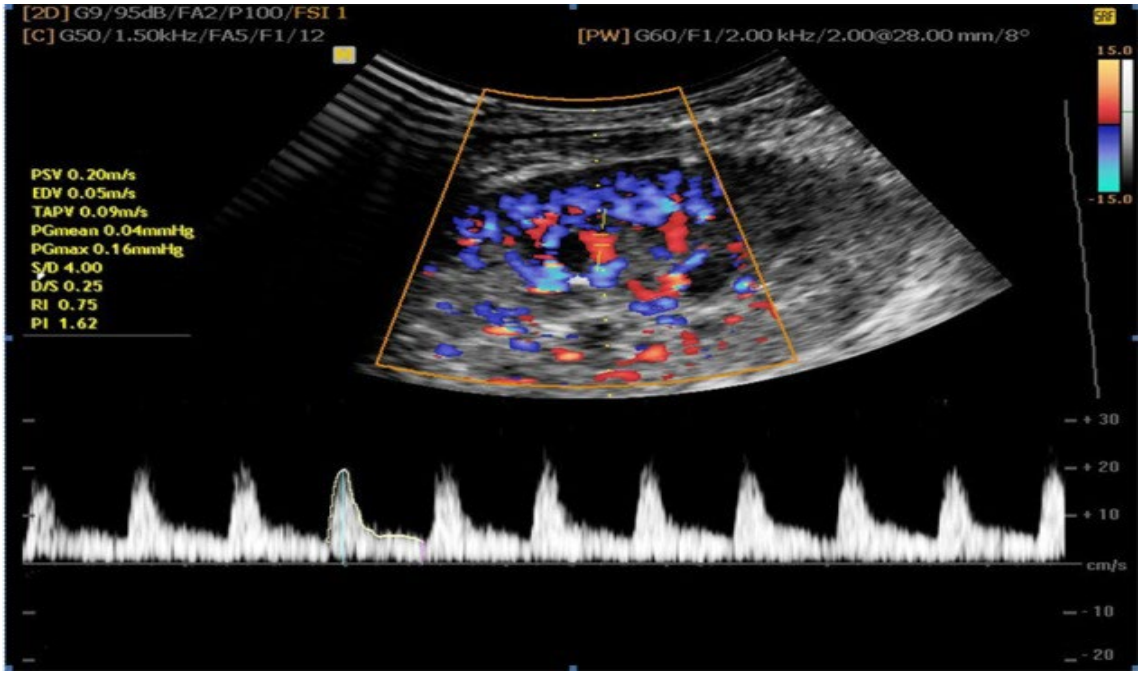

Figure 20. DUS image for inflow boundary conditions

Form DUS image data and parametric assumptions, the pressure gradients were assumed as follows,

Ps = 280.00 Pa/m.

P_0 = 488.3525 Pa/m.

The initial condition was considered a parabolic velocity profile. The boundary condition was assumed to be a periodical boundary condition at the inlet and outlet.

The analytical solution of the Womersley flow that was used for validating the results from ICFD outputs is as follows,

$$u(r,t) = \frac{P_s R^2}{4\mu}\left(1 - \frac{r^2}{R^2}\right) + \text{Real}\left\{\frac{P_o R^2}{i\mu\alpha^2}\left[1 - \frac{J_0\left(\frac{\alpha r}{R} i^{\frac{3}{2}}\right)}{J_0\left(\alpha i^{\frac{3}{2}}\right)}\right] e^{i\omega t}\right\}$$

Other input parameters used for the ICFD analysis are as follows:

For an average of 75 heartbeats per min, time-period of a human cardiac cycle,

T = 0.8 sec

angular frequency, $\omega = \frac{2\pi}{T} = 7.85\ s^{-1}$

kinematic viscosity of blood, $\mu = 3.415*10^{-6}\ m^2/s$

density of blood, $\rho = 1025\ kg/m^3$

Heart rate = HR beats/minute

So, $\omega = \pi \cdot HR/30$ sec^{-1}

Peak Systolic Velocity (PSV): V_{sys}

End Diastolic Velocity (EDV): V_{edv}

Resistive Index, RI $= \frac{V_{sys} - V_{edv}}{V_{sys}}$

Here, PSV and ESV are calculated after the ICFD simulation to measure the RI to quantify the relationship between the change of pulsatile parameters such as the pulsatile pressure gradient (P_0) or heart rate (HR) and resistive index (RI).

Discretization

In this case, the grid size in the x and y-direction of the pipe will be N_D along the diameter, and in the z-direction will be $10N_D$ along the length of the pipe. We created four different resolution cases by choosing a different number of cells in diameter or different grid numbers along the diameter. As we kept increasing the resolution, the physical length of the cells kept going down. As we have limited computational power, we could not take more than 115 cells in diameter for this case.

Table 3.1. This table shows the number of cells in each direction and their physical length

SL No.	Number of cells in x-direction (N_D)	Number of cells in y-direction (N_D)	Number of cells in z-direction $(10N_D)$	Physical length of a grid $\left(\Delta x = \frac{0.005}{N_D}\right) m$
1.	25	25	250	0.0002
2.	45	45	450	0.000111
3.	69	69	690	0.000072463
4.	115	115	1150	0.044173912380053

3.2.2 Parametrization for Stenosis Severity

Siemens NX was used to create stenosis inside the pipe. The degree of stenosis or stenosis severity was varied to conduct a parametric study to find the effect of stenosis severity on RI. In this study, five different cases of stenosis severity were considered. The geometries were generated from stenosis severity based on diameter. Afterward, the volume reduction was calculated from the volume analysis in Siemens NX.

Table 3.2. This table shows the stenosis percentage increase based on Diameter reduction and in terms of volume reduction

Case No.	Diameter reduction (S_D)	Volume reduction (S_V)
01	0%	0%
02	20%	4.04%
03	40%	12.91%
04	60%	20.66%
05	80%	34.27%

3.2.3 Post-processing

MATLAB and Tecplot were implemented for the post-processing of 4D velocity field data from the output of VLBM. For post-processing, one period of the pulsatile flow is divided into 4-time points. For each of these time points, velocity is measured at the longitudinal middle plane of

the 3D pipe geometry along its diameter. In this case, the time period is 0.8 sec, and so each time point is 0.2 sec apart.

3.2.4 Results and Validation

For validation, a convergence check was conducted to find the optimum resolution for the ICFD analysis. Next, velocity profiles from the ICFD results were compared against the analytical solution. Finally, the results from the parametric study were compared against the experimental results.

Convergence Check

A convergence check was performed by calculating the velocity at the center of the 3-D pipe of a specific time-point for all four resolutions. Next, the velocities were compared to each other, and the relative error was calculated.

Table 3.3. $Relative\ Error = \frac{|V_2 - V_1|}{V_1}$ where V_1 is the interested quantity at last resolution, and V_2 is the interested quantity at the current resolution.

Grid numbers in Diameter	Velocity at center	Relative Error
25	0.1827	-
45	0.1889	0.0339
69	0.1925	0.0191
115	0.1937	0.00623

As the 115-resolution case had the lowest relative error, it was selected as the resolution to conduct the subsequent several parametric studies.

Computed vs. Analytical Velocity Profiles

Velocity vs. Normalized radius comparison with the analytical solution for 115 cells in diameter spatial resolution case is shown in Figure 21. It shows the cross-section of the pipe and a line denoting in which location of the pipe this comparison was made. It also shows the four-time points on the pulsating time period for which the velocities were compared.

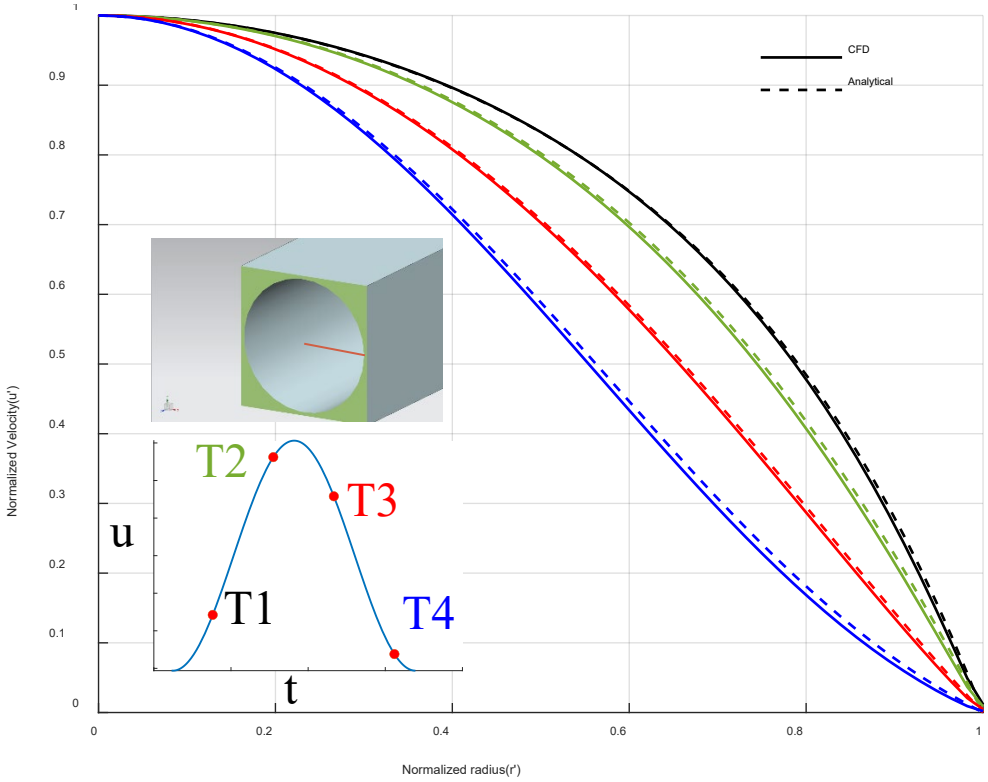

Figure 21. Validation: ICFD vs. Analytical velocity profiles

From Figure 21, we can see a good comparison between the ICFD data and analytical solutions for normalized velocity vs. normalized radius. Also, we can observe a minute deviation from the analytical solution at the very beginning and at the very end of the pulsatile time points. Table 3.4 shows this by calculating the Relative L^2 Error Norm for all the cells at those four-time points and compare with the analytical solutions.

Table 3.4. This table shows the Relative L^2 Error Norm for all the cells, and the formula used here, $Error = \sqrt{\frac{\sum(V_{num}-V_{ana})^2}{\sum {V_{ana}}^2}}$

Time-point	T1	T2	T3	T4
Error	0.005493	0.0066781	0.0051619	0.010641

Varying Pulsatility Magnitude and RI

For conducting the next part of the parametric study, we wanted to explore how the change of pulsatile parameters impacts resistive index RI. To do that, while keeping the heart rate (HR) the same (75 beats/minute), pulsatility magnitude (Po) varied from 288 -688 Pa/m. Moreover, we considered five different cases with different Po, found the PSV and EDV from the 4-D velocity field, and finally calculated RI for each of the five cases.

Table 3.5. This table shows the effect of pulsatility magnitude on RI with constant Heart Rate

Case No.	Heartbeats/min	Pulsatile pressure gradient (Po)	PSV	EDV	Resistive Index (RI)
01	75	288	0.1638	0.0752	0.54
02		388	0.1791	0.0599	0.67
03		488	0.1945	0.0446	0.77
04		588	0.2099	0.0293	0.86
05		688	0.2253	0.0140	0.94

We also compared our findings with the experimental work done in our group, which also explored similar effects of pulsatility index on RI.

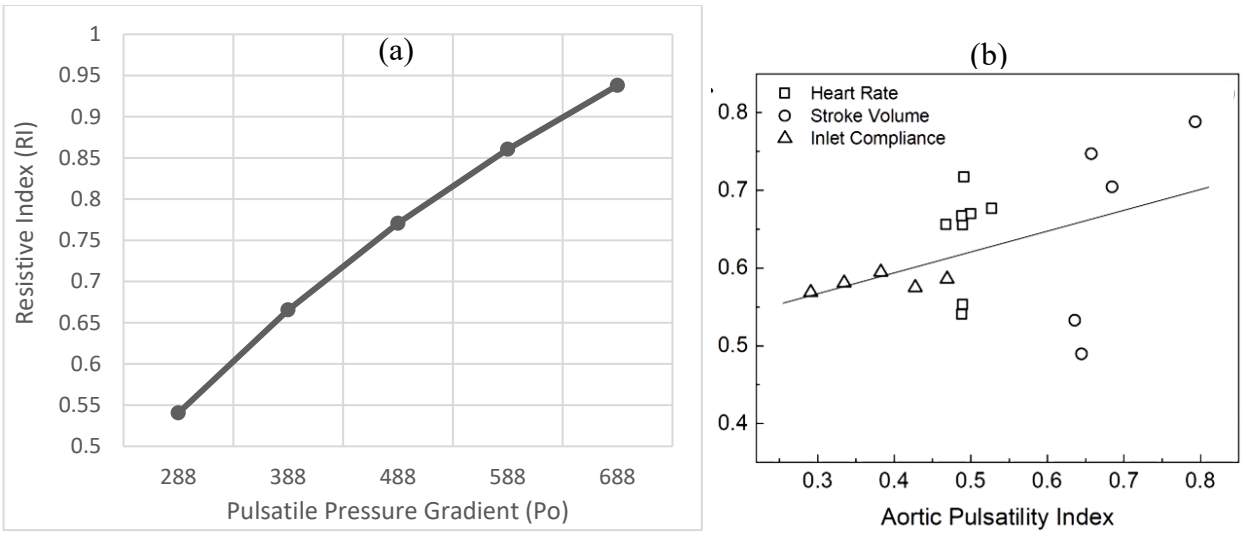

Figure 22. Resistive index (RI) vs. Pulsatility index for (a) ICFD analysis, (b) experimental analysis

In both ICFD analysis and experimental work, the trend shows that Resistive Index (RI) has a positive correlation with the increase of Pulsatile pressure gradient (Po).

Varying Heart Rate and RI

For this parametric study, we kept the pulsatility pressure magnitude the same (488.3525 Pa/m) and varied the heart rate (HR) from 56 -94 beats/minute.

Ps: Mean magnitude (280.00 Pa/m)

Po: Pulsatility magnitude (488.3525 Pa/m)

Angular frequency, $\omega = \frac{2\pi}{T}$

Heartbeat/min or Heart rate (HR): $= \frac{60}{T}$ beats/min $= \frac{60*\omega}{2\pi}$ beats/min

$= \frac{30*\omega}{\pi}$ beats/min

Resistive index, RI $= \frac{V_{sys} - V_{edv}}{V_{sys}}$

Table 3.6. This table shows the Effect of HR on RI when keeping the same pulsatility magnitude

Case No.	Pulsatility Magnitude (P_o)	Hear Rate (heartbeats/minute)	PSV(m/s)	EDV(m/s)	Resistive Index (RI)
01	488.3525	56	0.2176	0.0216	0.90
02		66	0.2049	0.0342	0.83
03		75	0.1945	0.0446	0.77
04		85	0.1859	0.0530	0.72
05		94	0.1787	0.0601	0.66

Similar to the previous parametric study, we also considered five different cases with different HR, found the PSV and EDV from the 4-D velocity field, and finally calculated RI for each of the five cases. We also compared our findings with the experimental work done in our group, which also explored similar effects of changing heart rate on RI.

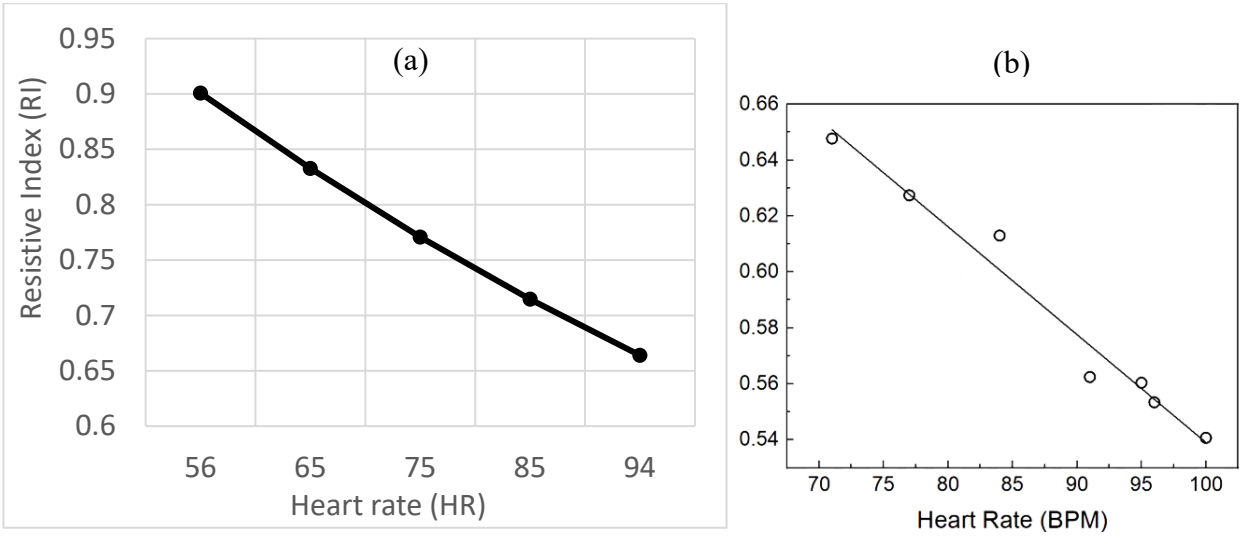

Figure 23. Resistive index (RI) vs. Heart rate for (a) ICFD analysis, (b) experimental analysis

In both ICFD analysis and experimental work, the trend indicates that Resistive Index (RI) shows a negative correlation with the increase in Heart Rate (HR).

Stenosis Severity and RI

In this parametric study, we explore the effects of change in stenosis severity on RI. The input parameters are,

Calculations were done for 75 heartbeats per minute.

So, the Time period for a cardiac cycle, T = $\frac{60}{75}$ sec = 0.8 sec

Angular frequency, ω = $\frac{2\pi}{T}$ = 7.85 s^{-1}

Heartbeat/min or Heart rate (HR): = $\frac{60*\omega}{2\pi}$ beats per min = $\frac{30*\omega}{\pi}$ beats per min

Po = 488.3525 Pa/m

Ps = 280.00 Pa/m

RI = $\frac{V_{sys} - V_{edv}}{V_{sys}}$

Using these parameters, we conducted ICFD analysis for five different stenosis severity cases 0%, 20%, 40%, 60%, and 80% stenosis severity based on diameter. Then we calculated PSV, EDV, and finally RI at three different distances from the inlet and outlet, at 5mm, 10mm, and 20mm distances. The following sections describe the results for each of these cases.

Case One

For this case, the calculations were done at a 5 mm distance from the inlet and the outlet of the 3-D pipe. Figure 24 shows the longitudinal section view of a pipe with stenosis and the locations where the PSV and EDV velocities were measured to calculate the RI.

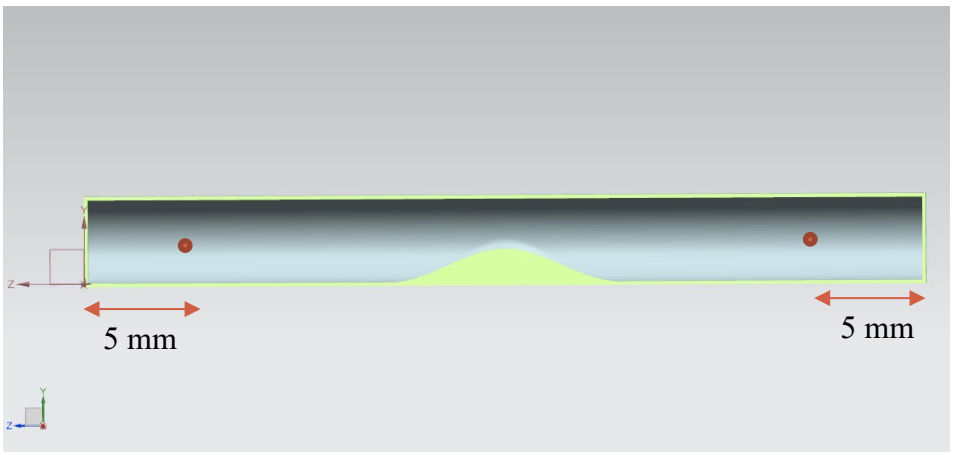

Figure 24. Longitudinal-section of pipe with stenosis for calculating RI at 5 mm distance from inlet and outlet

Table 3.7 shows the measurements of PSV and EDV made at the aforementioned locations before and after stenosis. It also shows the stenosis severity in both S_D and S_V and also calculates the RI for each case.

Table 3.7. This table shows the relationship between RI and Stenosis severity at a 5 mm distance from the inlet and outlet of the 3-D pipe

Case No.	S_D	S_V	Before Stenosis			After Stenosis		
			PSV	EDV	RI	PSV	EDV	RI
01	0%	0%				0.1945	0.0446	0.7707
02	20%	4.04%	0.1915	0.0428	0.7764	0.1925	0.0429	0.7772
03	40%	12.91%	0.1689	0.0298	0.8239	0.1761	0.0301	0.8292
04	60%	20.66%	0.1099	0.0037	0.9662	0.1225	0.0040	0.9671
05	80%	34.27%	0.0260	0.00	1.0	0.0261	0.00	1.0

Figure 25 shows the five different stenosis severity S_D and their respective RI. In the figure, the solid black line denotes the RI before the stenosis. Furthermore, the red dotted line shows the RI after the stenosis.

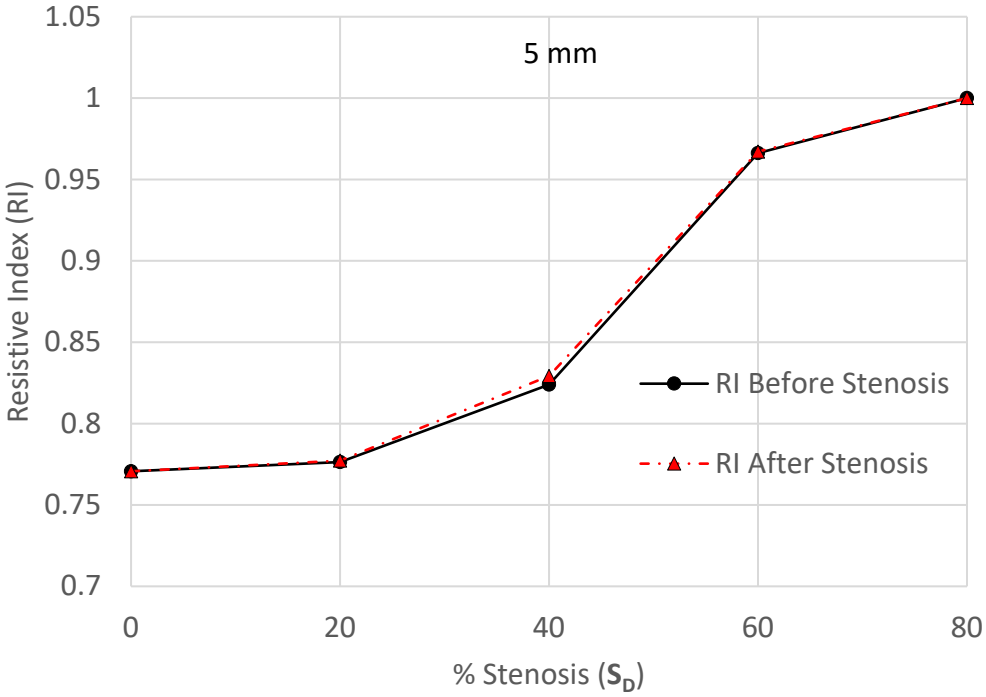

Figure 25. Resistive index (RI) vs. Stenosis severity

Table 3.7 and figure 25 show that RI increases when Stenosis severity increases, and after and S_D of 40%, RI rises sharply. Also, we can observe that the differences in RI before and after the stenosis is not much, while we can observe the most difference at 40% of S_D.

Case Two

For this case, the calculations were done at a 10 mm distance from the inlet and the outlet of the 3-D pipe. Figure 26 shows the longitudinal section view of a pipe with stenosis and the locations where the PSV and EDV velocities were measured to calculate the RI.

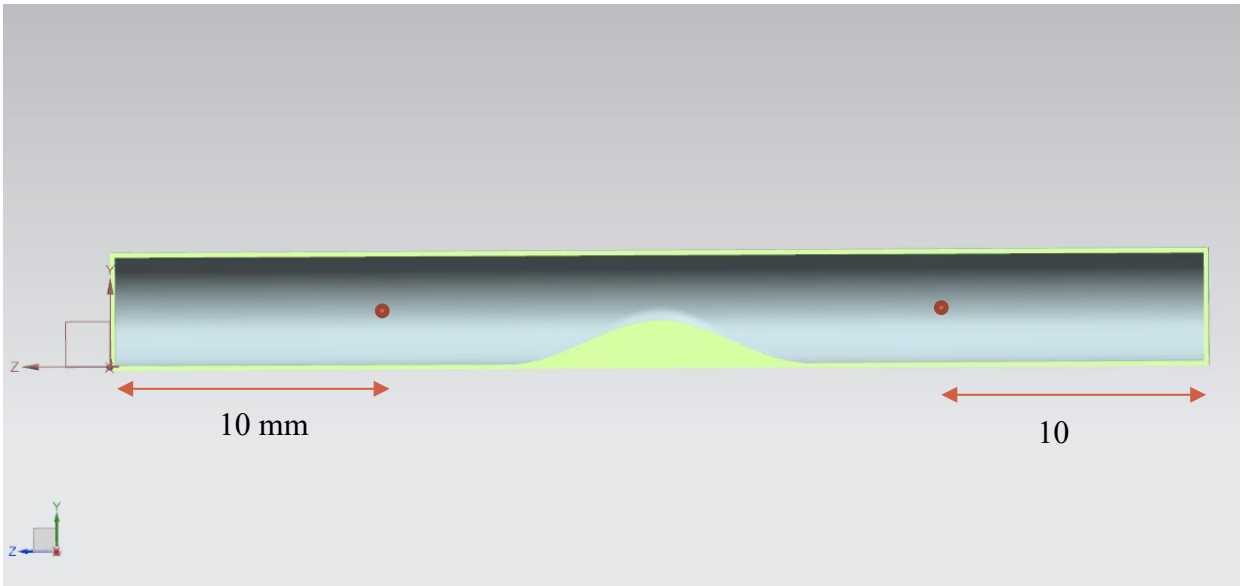

Figure 26. Longitudinal-section of pipe with stenosis for calculating RI at 10 mm distance from inlet and outlet

Table 3.8 shows the measurements of PSV and EDV made at the locations specified previously before and after stenosis. It also shows the stenosis severity in both S_D and S_V and calculates the RI for each case.

Table 3.8. This table shows the relationship between RI and Stenosis severity at a 10 mm distance from the inlet and outlet of the 3-D pipe

Case No.	S_D	S_V	Before Stenosis			After Stenosis		
			PSV	EDV	RI	PSV	EDV	RI
01	0%	0%				0.1945	0.0446	0.7707
02	20%	4.04%	0.1913	0.0428	0.7763	0.1933	0.0429	0.7779
03	40%	12.91%	0.1675	0.0297	0.8230	0.1830	0.0305	0.8331
04	60%	20.66%	0.1098	0.0036	0.9671	0.1445	0.0048	0.9667
05	80%	34.27%	0.0271	0.00	1.0	0.0298	0.00	1.0

Figure 27 shows the five different stenosis severity S_D and their respective RI. In the figure, the solid black line denotes the RI before the stenosis. Moreover, the red dotted line shows the RI after the stenosis.

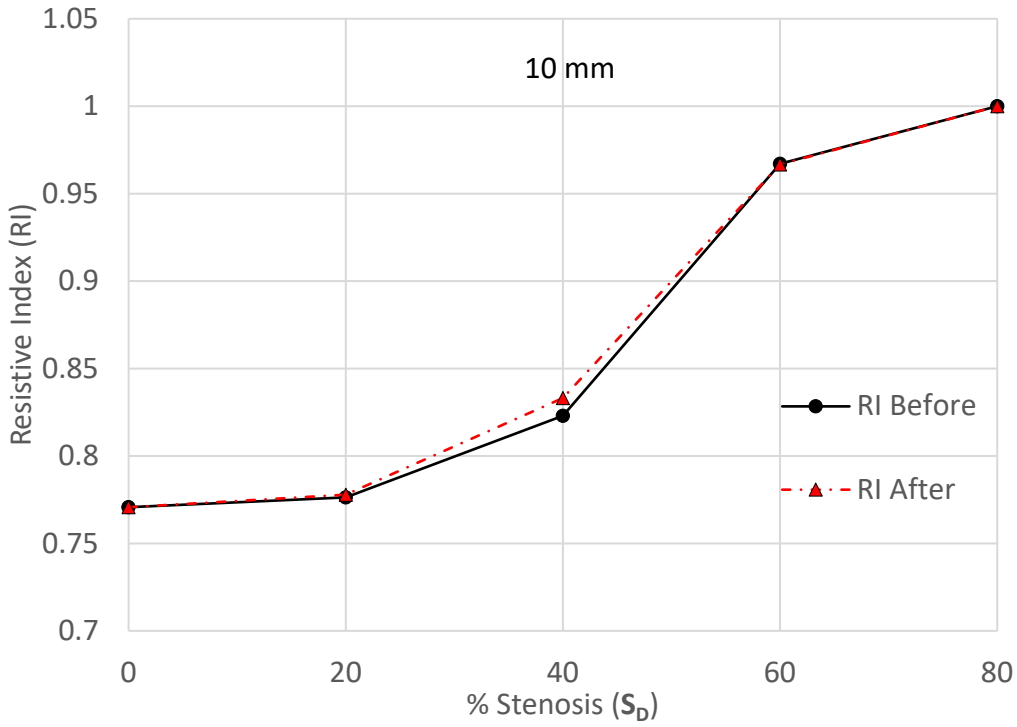

Figure 27. Resistive index (RI) vs. Stenosis severity

Table 3.8 and figure 27 also show that RI increases when Stenosis severity increases, and after and S_D of 40%, RI rises sharply. We can also observe that the deviations in RI before and after the stenosis have increased a little compared to the previous 5 mm distance case, while we can still observe the most difference at 40% of S_D.

Case Three

Finally, for this case, the calculations were done at a 20 mm distance from the inlet and the outlet of the 3-D pipe. Figure 26 shows the longitudinal section view of a pipe with stenosis and the locations where the PSV and EDV velocities were measured to calculate the RI.

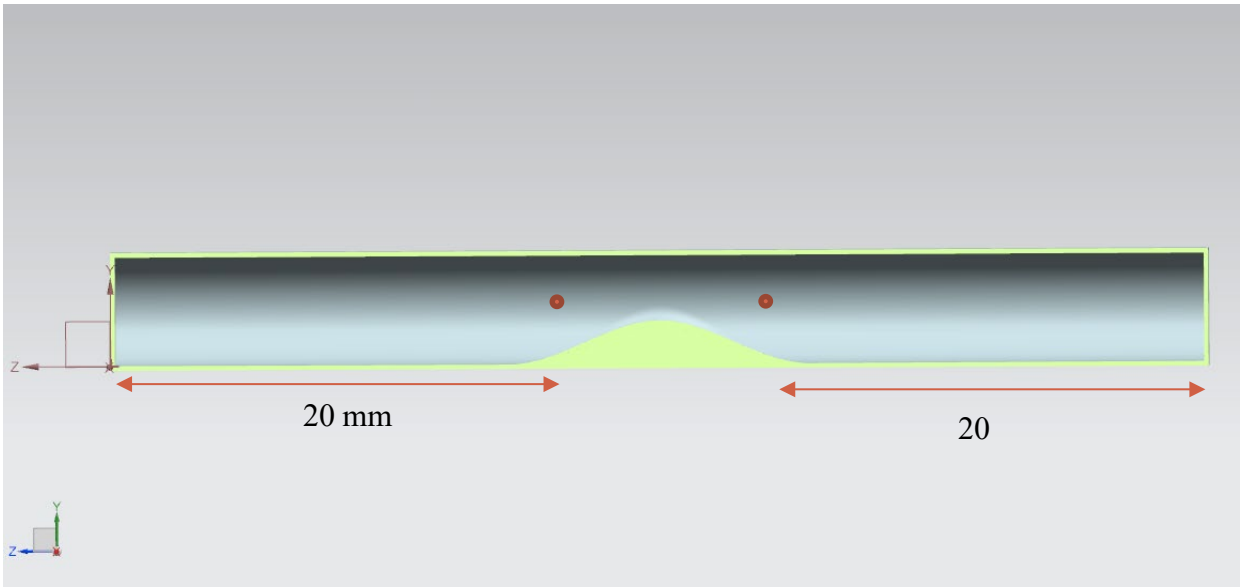

Figure 28. Longitudinal-section of pipe with stenosis for calculating RI at 20 mm distance from inlet and outlet

Table 3.9 shows the measurements of PSV and EDV made at the locations specified previously before and after stenosis. It also shows the stenosis severity in both S_D and S_V and calculates the RI for each case.

Table 3.9. This table shows the relationship between RI and Stenosis severity at a 20 mm distance from the inlet and outlet of the 3-D pipe

Case No.	S_D	S_V	**Before Stenosis**			**After Stenosis**		
			PSV	**EDV**	**RI**	**PSV**	**EDV**	**RI**
01	0%	0%				0.1945	0.0446	0.7707
02	20%	4.04%	0.1910	0.0428	0.7762	0.1960	0.0432	0.7797
03	40%	12.91%	0.1684	0.0297	0.8238	0.1994	0.0310	0.8444
04	60%	20.66%	0.1271	.00066	0.9948	0.1997	0.0029	0.9854
05	80%	34.27%	0.0691	0.00	1.0	0.1035	0.00	1.0

Figure 29 shows the five different stenosis severity S_D and their respective RI. In the figure, the solid black line denotes the RI before the stenosis. Furthermore, the red dotted line shows the RI after the stenosis.

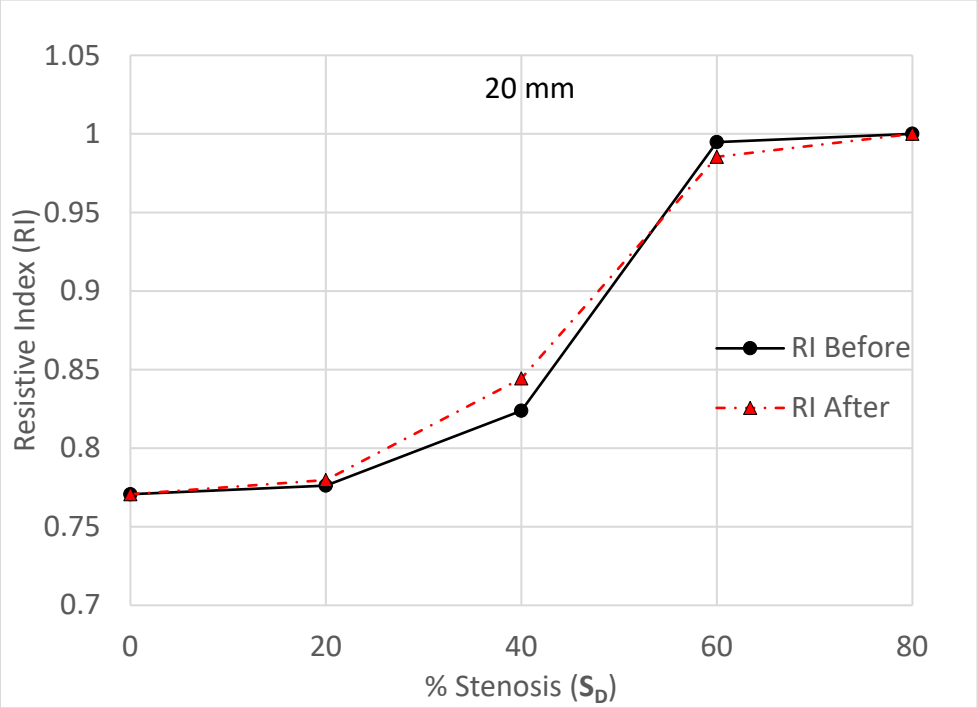

Figure 29. Resistive index (RI) vs. Stenosis severity

Table 3.9 and figure 29 also show that RI increases when Stenosis severity increases, and after and S_D of 40%, RI rises very sharply. We also observed that the differences in RI before and after the stenosis had increased a lot more compared to the previous 5 mm, 10 mm distance cases. We can observe a significant difference at 20% and 60% S_D while we still find the most deviation at 40% of S_D.

This parametric study shows that resistive index RI has a positive correlation with the increase in stenosis severity S_D as well as S_V.

3.3 Surrogate Model

In this work, we created surrogate models for predicting the velocity field inside an image-based 3D pipe geometry for both Hagen-Poiseuille flow and Womersley flow using Gaussian Process Regression in MATLAB Machine Learning Toolbox. We used the software package DACE (Design and Analysis of Computer Experiments), which is a MATLAB toolbox for working with kriging approximations to computer models, for creating the GPR surrogate models for both Hagen-Poiseuille flow and Womersley flows in this work.

Training Dataset Generation

For creating the surrogate model, the first step is to create training datasets that will be used to train the surrogate models. In this work, we used analytical solutions to generate a training dataset for both the surrogate models. For Hagen-Poiseuille flow in a pipe, the analytical solution is as follows,

$$u_r = \frac{u_{max}}{R^2}(R^2 - r^2)$$

This equation was used to create the training dataset and testing dataset for training and evaluating the accuracy of the surrogate model, respectively.

Range for u_{max} was $0.1 \sim 5\ m/s, and\ R = 0.0025\ m$. The number of training data points for the surrogate model was 450.

Moreover, for pulsatile flow, the Womersley equation was used to create a training dataset and a test dataset to train the surrogate model and calculate the accuracy of predictions of the model. The analytical solution for Womersley flow is as follows,

$$\frac{u}{u_{max}} = \left(1 - \frac{r^2}{R^2}\right) + \frac{4A}{\alpha^2} Real\left\{\frac{1}{i}\left[1 - \frac{J_0(\frac{\alpha r}{R} i^{\frac{3}{2}})}{J_0(\alpha i^{\frac{3}{2}})}\right] e^{i\omega t}\right\}$$

The normalized analytical solution is,

$$u'(r', t') = (1 - r'^2) + \frac{4A}{\alpha^2} Real\left\{\frac{1}{i}\left[1 - \frac{J_0\left(\alpha r' i^{\frac{3}{2}}\right)}{J_0\left(\alpha i^{\frac{3}{2}}\right)}\right] e^{it'}\right\}$$

where, $t' = \omega t$

Here we considered, $\omega = 7.85$ sec^{-1}

And range for pulsatile time-period, t = (0.604 ~ 1.304) sec

So, $t' = \omega t$ = 7.85 *(0.604 ~ 1.304) = 4.7414 ~ 10.2364

Therefore, for the surrogate model input ranges were,

A: $1 \sim 2$

α: $2 \sim 5$

r': $0 \sim 1$,

t': 4.7414 ~ 10.2364

The number of training data points for the surrogate model was 9000.

Training Surrogate Model

For training the models, first, the input and output parameters were specified for each flow. In both cases, we specified the velocity field u as output. All the other parameters were assumed as inputs or constants for simplification. Next, a range was specified for each input variable, and a normal distribution of randomly generated inputs within that specified range was taken. Finally, the analytical solutions of both flows were used to find the output u for a random combination of those input parameters. Thus, the training datasets were generated for each model.

After the training dataset was generated, both the surrogate models were trained using a specific training dataset. The surrogate model for the Hagen-Poiseuille flow required less training data compared to the model for pulsatile flow to reach the required goal of prediction accuracy as the number of input parameters is far less compared to Womersley flow.

Validation

For testing the accuracy of the predictions from the surrogate models, new datasets were generated using the analytical solutions of both flows. The testing dataset also had inputs within the same range of training dataset inputs. The testing dataset was also generated using a normal distribution of the specified range and a random number generation algorithm from MATLAB. Finally, when the surrogate models achieved good comparison, they were used to make predictions for the same input parameters as ICFD results.

In this work, we compared the surrogate model predictions with both ICFD results and analytical solutions for both Hagen-Poiseuille and Womersley flows.

3.3.1 Hagen-Poiseuille Flow Model

For validation, normalized velocity vs. normalized radius results was compared from the trained surrogate model predictions with both ICFD and Analytical data.

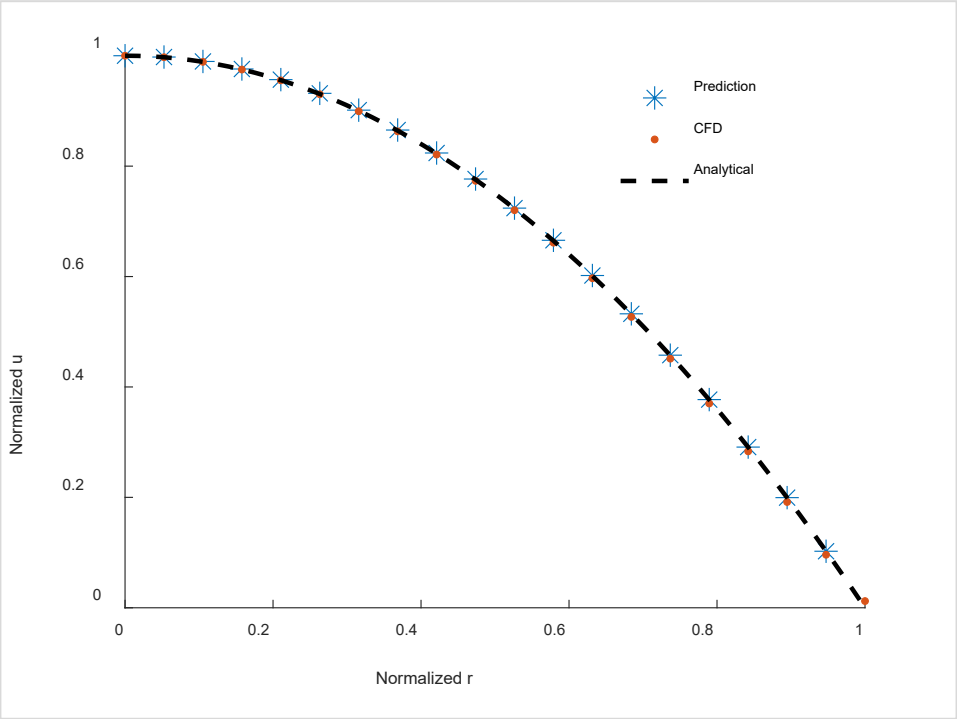

Figure 30. Validation for the surrogate model of Hagen-Poiseuille flow

$$\text{Prediction Error} = \sqrt{\frac{\Sigma(V_{pred}-V_{ana})^2}{\Sigma {V_{ana}}^2}} = 0.11\%$$

$$\text{ICFD Error} = \sqrt{\frac{\Sigma(V_{CFD}-V_{ana})^2}{\Sigma {V_{ana}}^2}} = 0.59\%$$

The surrogate model prediction is equally well to the ICFD results when compared with the analytical solution for Hagen-Poiseuille flow. When compared against the analytical solution, a prediction error of 0.11% was observed, whereas the CFD error was 0.59%.

3.3.2 Womersley Flow Model

For validation of the trained surrogate model, the normalized velocity for four different time stamps of a pulse period of Womersley flow vs. normalized radius results was compared with both ICFD results at the same time points and locations and analytical solutions.

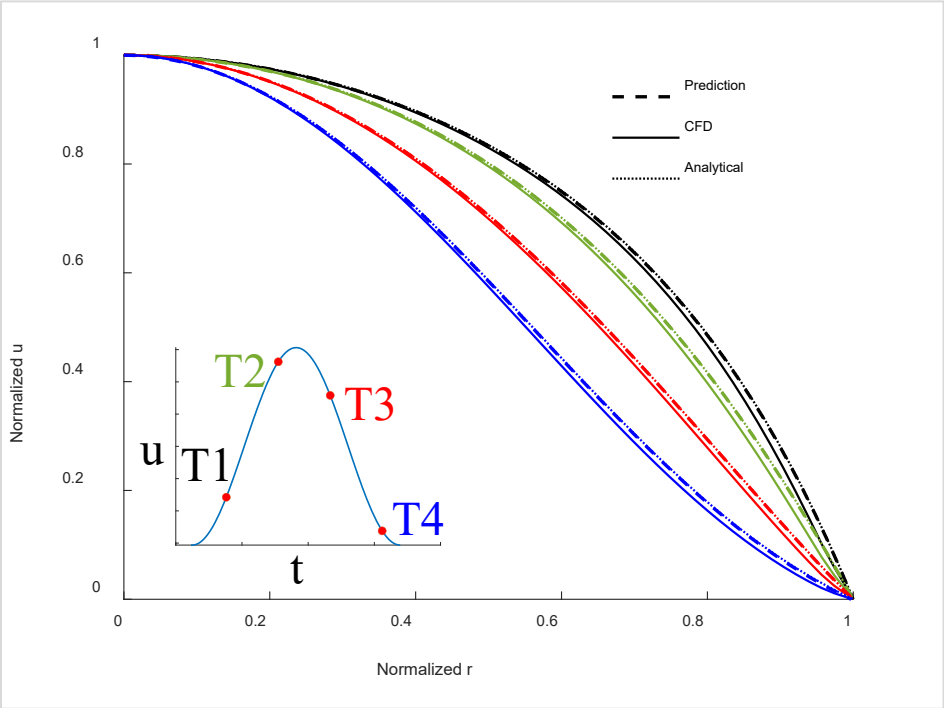

Figure 31. Validation for the surrogate model of Womersley flow

$$\text{Prediction Error} = \sqrt{\frac{\Sigma(V_{pred}-V_{ana})^2}{\Sigma {V_{ana}}^2}} = 0.53\%$$

$$\text{ICFD Error} = \sqrt{\frac{\Sigma(V_{CFD}-V_{ana})^2}{\Sigma {V_{ana}}^2}} = 0.63\%$$

Surrogate model predictions for Womersley flow at representative time points in a pulse are in good agreement with analytical solutions and CFD simulation results. Compared to the analytical solution, a mean error of 0.53% was found, whereas the CFD error was determined as 0.63%.

4. SUMMARY

In this study, 3-D reconstruction of several human vessel systems was established. We also developed a MATLAB code to perform image processing of SEM data and 3-D construction of choriocapillaris. We also created several idealized vessel geometries for parametric study using commercial CAD packages.

We also conducted several parametric studies to ensure the reliability and applicability of our ICFD solver *InVascular* and our computational method. We conducted convergence checks and validations and found that the velocity profiles from the results agree with the analytical solution of the Womersley flow. We also explored the effects of the Pulsatility index and heart rate on RI and observed that RI has a positive correlation with the increase of pulsatile pressure gradient and a negative correlation with the increase of heart rate, which is consistent with experimental results. We also found from our parametric studies that; severer stenosis corresponds to larger RI. These results show that, besides pressure gradient-based indices, this velocity-based index, RI, can be a good indication of stenosis severity.

In this work, we also implemented supervised machine learning to create surrogate models to achieve extremely fast ICFD results compared to traditional ICFD solvers. We used a Gaussian Process Regression model, DACE, to create surrogate models for both Hagen-Poiseuille and Womersley flows. After completion of model training, we compared the prediction results from the surrogate models against both ICFD results and analytical solutions. For the surrogate model of Hagen-Poiseuille flow, a prediction error of 0.11% was observed, whereas the ICFD error was 0.59% when compared to the analytical solution. Furthermore, for the surrogate model of Womersley flow, a mean error of 0.53% was found, whereas the CFD error was determined as 0.63% when compared to the analytical solution. Therefore, we can conclude that the surrogate models can precisely represent both Hagen-Poiseuille and Womersley flow models.

APPENDIX

I.MATLAB code: Image Processing from RAW 8-bit RGB to Binary Image Data

```
clc; clear; clear all;

Raw_image = imread('Raw.tif'); %Import Raw image

image = rgb2gray(Raw_image);    %Convert raw image to grayscale

binary_image = imbinarize(image); %Binarize Image Using Global Threshold
imshow(binary_image)

BW = imbinarize(image, 'adaptive'); %Binarize Image Using Locally Adaptive
Thresholding

mean_Intensity = mean(image,'all');   %Determine the mean value of pixels in the
grayscale image.
binary_mean = image > mean_Intensity;

mean_user = input('Enter a threshold value within 0 to 255. \n');  %Taking input for
Threshold
binary_user = image > mean_user;

imshowpair(binary_user,BW,'montage')

subplot(1,4,1);
imshow(Raw_image);
title('Original Image');

subplot(1,4,2);
imshow(BW);
title('Adaptive');

subplot(1,4,3);
imshow(binary_mean);
title('Mean Intensity');

subplot(1,4,4);
imshow(binary_user);
title('User Input');

imwrite(BW,'Adapdive_thresholding.tif'); %Saving converted binary image to a file
imwrite(binary_mean,'Mean_intensity.tif');
imwrite(binary_user,'User_input.tif');
```

II. MATLAB code: Binary Image in Thresholding Method and Cleaning up

```
Raw_image = imread('Raw.tif'); %Import Raw image
[J,rect] = imcrop(Raw_image);
image = rgb2gray(Raw_image);    %Convert raw image to grayscale

mean_user = input('Enter a threshold value within 0 to 255. \n');  %Taking input for
Threshold
binary_user = image > mean_user;

% imshowpair(binary_user,BW,'montage')

imwrite(binary_user,'User_input.tif');

%Cleaning binary iamge
%Method 1
% b0 = bwmorph(binary_user,'majority');
% b1 = bwmorph(b0,'clean');    %Removes isolated pixels
% b2 = bwareaopen(b1, 2);    %Remove objects containing fewer than 5 pixels
% b3 = bwmorph(b2,'fill');    %Fills isolated interior pixels

%Method 2
% b0 = bwmorph(binary_user,'majority');
b1 = bwmorph(binary_user,'clean');    %Removes isolated pixels
b2 = bwareaopen(b1, 5);    %Remove objects containing fewer than 5 pixels
b3 = bwmorph(b2,'fill');    %Fills isolated interior pixels

imwrite(b3,'Binary.tif');
```

III. MATLAB code: Thresholding Method from RAW 16-bit RGB to Cropped Binary Image and Cleaning up

```
clc; clear; clearvars;

I = imread('18-0814 OS  LIPA for WY.tif'); %Import Raw image

[J,rect] = imcrop(I);   %Crop raw image
% imshow(J)
imwrite(J,'Raw_cropped.tif');   %save cropped raw image

% K = rgb2gray(J);    %covert rgb to grayscale
% imwrite(K,'Gray_cropped.tif');   %save cropped raw image
img8 = uint8(J / 256);
user_input = input('Enter a threshold value within 0 to 255. \n');  %Taking input for
Threshold
binary_user = img8 > user_input;
% imshow(binary_user)
imwrite(binary_user,'Binary_user.tif');  %save binary image

%Cleaning binary iamge
%Method 1
% b0 = bwmorph(binary_user,'majority');
% b1 = bwmorph(b0,'clean');    %Removes isolated pixels
% b2 = bwareaopen(b1, 2);    %Remove objects containing fewer than 5 pixels
```

```
% b3 = bwmorph(b2,'fill');    %Fills isolated interior pixels

%Method 2
% b0 = bwmorph(binary_user,'majority');
b1 = bwmorph(binary_user,'clean');    %Removes isolated pixels
b2 = bwareaopen(b1, 5);    %Remove objects containing fewer than 5 pixels
b3 = bwmorph(b2,'fill');    %Fills isolated interior pixels

imwrite(b3,'Binary.tif');
% M = imread('Manual.tif');
% imshowpair(M,b3,'montage')
% imshowpair(J,K,'montage')
```

REFERENCES

1 Chen, R., Yu, H. & Zhu, L. Effects of initial conditions on the coalescence of micro-bubbles. *Proceedings of the Institution of Mechanical Engineers, Part C: Journal of Mechanical Engineering Science* **232**, 457-465, doi:10.1177/0954406217742941 (2018).

2 Sawchuk, A. P. *et al.* Noninvasive Measurement of Renovascular Resistance and the Meaning and Limitations of the Renal Resistance Index. *Journal of Vascular Surgery* **64**, 876-877, doi:10.1016/j.jvs.2016.07.030 (2016).

3 Frank, A. O., Walsh, P. W. & Moore, J. E., Jr. Computational fluid dynamics and stent design. *Artif Organs* **26**, 614-621, doi:10.1046/j.1525-1594.2002.07084.x (2002).

4 Fraser, K. H., Taskin, M. E., Griffith, B. P. & Wu, Z. J. The use of computational fluid dynamics in the development of ventricular assist devices. *Med Eng Phys* **33**, 263-280, doi:10.1016/j.medengphy.2010.10.014 (2011).

5 Morris, P. D. *et al.* Computational fluid dynamics modelling in cardiovascular medicine. *Heart* **102**, 18-28, doi:10.1136/heartjnl-2015-308044 (2016).

6 Lin, C. L., Tawhai, M. H. & Hoffman, E. A. Multiscale image-based modeling and simulation of gas flow and particle transport in the human lungs. *Wiley Interdiscip Rev Syst Biol Med* **5**, 643-655, doi:10.1002/wsbm.1234 (2013).

7 Burrowes, K. S., De Backer, J. & Kumar, H. Image-based computational fluid dynamics in the lung: virtual reality or new clinical practice? *Wiley Interdiscip Rev Syst Biol Med* **9**, doi:10.1002/wsbm.1392 (2017).

8 Wendt, J. F., Anderson, J. D. & Von Karman Institute for Fluid Dynamics. *Computational fluid dynamics : an introduction*. 3rd edn, (Springer, 2008).

9 Chung, T. J. & ProQuest. *Computational fluid dynamics*. Second edition. edn, (Cambridge University Press, 2010).

10 Morris, P. D. *et al.* Computational fluid dynamics modelling in cardiovascular medicine. *Heart* **102**, 18-28 (2016).

11 Marsden, A. L. & Esmaily-Moghadam, M. Multiscale modeling of cardiovascular flows for clinical decision support. *Applied Mechanics Reviews* **67** (2015).

12 Zhang, J. M. *et al.* Perspective on CFD studies of coronary artery disease lesions and hemodynamics: a review. *International journal for numerical methods in biomedical engineering* **30**, 659-680 (2014).

13 Shi, Y., Lawford, P. & Hose, R. Review of zero-D and 1-D models of blood flow in the cardiovascular system. *Biomedical engineering online* **10**, 1-38 (2011).

14 Taylor, C. A. & Figueroa, C. Patient-specific modeling of cardiovascular mechanics. *Annual review of biomedical engineering* **11**, 109-134 (2009).

15 Withey, D. J. & Koles, Z. J. A review of medical image segmentation: methods and available software. *International Journal of Bioelectromagnetism* **10**, 125-148 (2008).

16 Taylor, C. A. & Draney, M. T. Experimental and computational methods in cardiovascular fluid mechanics. *Annu. Rev. Fluid Mech.* **36**, 197-231 (2004).

17 Diagbouga, M. R., Morel, S., Bijlenga, P. & Kwak, B. R. Role of hemodynamics in initiation/growth of intracranial aneurysms. *European Journal of Clinical Investigation* **48**, e12992 (2018).

18 Gijsen, F. *et al.* Expert recommendations on the assessment of wall shear stress in human coronary arteries: existing methodologies, technical considerations, and clinical applications. *European heart journal* **40**, 3421-3433 (2019).

19 Arzani, A. & Shadden, S. C. Wall shear stress fixed points in cardiovascular fluid mechanics. *Journal of biomechanics* **73**, 145-152 (2018).

20 Acuna, A. *et al.* Computational Fluid Dynamics of Vascular Disease in Animal Models. *J Biomech Eng* **140**, doi:10.1115/1.4039678 (2018).

21 Steinman, D. A., Milner, J. S., Norley, C. J., Lownie, S. P. & Holdsworth, D. W. Image-based computational simulation of flow dynamics in a giant intracranial aneurysm. *AJNR Am J Neuroradiol* **24**, 559-566 (2003).

22 Ishida, F. *et al.* Computational Fluid Dynamics for Cerebral Aneurysms in Clinical Settings. *Acta Neurochir Suppl* **132**, 27-32, doi:10.1007/978-3-030-63453-7_4 (2021).

23 Fukazawa, K. *et al.* Using computational fluid dynamics analysis to characterize local hemodynamic features of middle cerebral artery aneurysm rupture points. *World Neurosurg* **83**, 80-86, doi:10.1016/j.wneu.2013.02.012 (2015).

24 Tsuji, M. *et al.* Stagnation and complex flow in ruptured cerebral aneurysms: a possible association with hemostatic pattern. *J Neurosurg* **126**, 1566-1572, doi:10.3171/2016.3.JNS152264 (2017).

25 Takao, H. *et al.* Hemodynamic differences between unruptured and ruptured intracranial aneurysms during observation. *Stroke* **43**, 1436-1439, doi:10.1161/STROKEAHA.111.640995 (2012).

26 Omodaka, S. *et al.* Local hemodynamics at the rupture point of cerebral aneurysms determined by computational fluid dynamics analysis. *Cerebrovasc Dis* **34**, 121-129, doi:10.1159/000339678 (2012).

27 Steinman, D. A. Image-based computational fluid dynamics modeling in realistic arterial geometries. *Ann Biomed Eng* **30**, 483-497, doi:10.1114/1.1467679 (2002).

28 Malek, A. M., Alper, S. L. & Izumo, S. Hemodynamic shear stress and its role in atherosclerosis. *JAMA* **282**, 2035-2042, doi:10.1001/jama.282.21.2035 (1999).

29 Friedman, M. H. & Deters, O. J. Correlation among shear rate measures in vascular flows. *J Biomech Eng* **109**, 25-26, doi:10.1115/1.3138637 (1987).

30 Steinman, D. A. Image-based computational fluid dynamics: a new paradigm for monitoring hemodynamics and atherosclerosis. *Curr Drug Targets Cardiovasc Haematol Disord* **4**, 183-197, doi:10.2174/1568006043336302 (2004).

31 Gerrah, R., Haller, S. J. & George, I. Mechanical Concepts Applied in Congenital Heart Disease and Cardiac Surgery. *Ann Thorac Surg* **103**, 2005-2014, doi:10.1016/j.athoracsur.2017.01.068 (2017).

32 Gerrah, R. & Haller, S. J. Computational fluid dynamics: a primer for congenital heart disease clinicians. *Asian Cardiovasc Thorac Ann* **28**, 520-532, doi:10.1177/0218492320957163 (2020).

33 Siallagan, D. *et al.* Virtual surgical planning, flow simulation, and 3-dimensional electrospinning of patient-specific grafts to optimize Fontan hemodynamics. *J Thorac Cardiovasc Surg* **155**, 1734-1742, doi:10.1016/j.jtcvs.2017.11.068 (2018).

34 Organization, W. H. The top 10 causes of death fact sheet. *World Health Organization*, 2018 (2017).

35 Pinto-Plata, V. M., Cote, C., Cabral, H., Taylor, J. & Celli, B. R. The 6-min walk distance: change over time and value as a predictor of survival in severe COPD. *Eur Respir J* **23**, 28-33, doi:10.1183/09031936.03.00034603 (2004).

36 Vignon-Clementel, I. E., Figueroa, C. A., Jansen, K. E. & Taylor, C. A. Outflow boundary conditions for three-dimensional finite element modeling of blood flow and pressure in arteries. *Computer methods in applied mechanics and engineering* **195**, 3776-3796 (2006).

37 Vignon-Clementel, I. E., Figueroa, C., Jansen, K. & Taylor, C. Outflow boundary conditions for 3D simulations of non-periodic blood flow and pressure fields in deformable arteries. *Computer methods in biomechanics and biomedical engineering* **13**, 625-640 (2010).

38 Formaggia, L., Lamponi, D. & Quarteroni, A. One-dimensional models for blood flow in arteries. *Journal of engineering mathematics* **47**, 251-276 (2003).

39 Benzi, R., Succi, S. & Vergassola, M. The lattice Boltzmann equation: theory and applications. *Physics Reports* **222**, 145-197 (1992).

40 Succi, S., Foti, E. & Higuera, F. Three-dimensional flows in complex geometries with the lattice Boltzmann method. *EPL (Europhysics Letters)* **10**, 433 (1989).

41 An, S., Yu, H. W. & Yao, J. GPU-accelerated volumetric lattice Boltzmann method for porous media flow. *Journal of Petroleum Science and Engineering* **156**, 546-552 (2017).

42 Yu, H. *et al.* Mass-conserved volumetric lattice Boltzmann method for complex flows with willfully moving boundaries. *Physical Review E* **89**, 063304 (2014).

43 Chen, R., Yu, H., Zhu, L., Patil, R. M. & Lee, T. Spatial and temporal scaling of unequal microbubble coalescence. *AIChE Journal* **63**, 1441-1450 (2017).

44 Wang, Z., Zhao, Y., Sawchuck, A. P., Dalsing, M. C. & Yu, H. W. GPU acceleration of Volumetric Lattice Boltzmann Method for patient-specific computational hemodynamics. *Computers & Fluids* **115**, 192-200 (2015).

45 Bastanlar, Y. & Ozuysal, M. Introduction to machine learning. *Methods Mol Biol* **1107**, 105-128, doi:10.1007/978-1-62703-748-8_7 (2014).

46 Wang, Z., Zhao, Y., Yu, H. W., Lin, C. & Sawchuck, A. P. Fully parallelized Lattice Boltzmann scheme for fast extraction of biomedical geometry. *Journal of Parallel and Distributed Computing* **128**, 126-136 (2019).

47 Domb, C. *Phase transitions and critical phenomena*. (Elsevier, 2000).

48 Kamio, T., Suzuki, M., Asaumi, R. & Kawai, T. DICOM segmentation and STL creation for 3D printing: a process and software package comparison for osseous anatomy. *3D Printing in Medicine* **6**, 1-12 (2020).

49 Fedorov, A. *et al.* 3D Slicer as an image computing platform for the Quantitative Imaging Network. *Magn Reson Imaging* **30**, 1323-1341, doi:10.1016/j.mri.2012.05.001 (2012).

50 An, S., Yu, H. W., Wang, Z., Kapadia, B. & Yao, J. Unified mesoscopic modeling and GPU-accelerated computational method for image-based pore-scale porous media flows. *International Journal of Heat and Mass Transfer* **115**, 1192-1202 (2017).

51 Yu, H. W. *et al.* GPU accelerated lattice Boltzmann simulation for rotational turbulence. *Computers & Mathematics with Applications* **67**, 445-451 (2014).

52 Jiang, F., Yang, J., Boek, E. & Tsuji, T. Investigation of viscous coupling effects in three-phase flow by lattice Boltzmann direct simulation and machine learning technique. *Advances in Water Resources* **147**, 103797 (2021).

53 Jiang, F. & Tsuji, T. Estimation of three-phase relative permeability by simulating fluid dynamics directly on rock-microstructure images. *Water Resources Research* **53**, 11-32 (2017).

54 Jiang, F., Tsuji, T. & Hu, C. Elucidating the role of interfacial tension for hydrological properties of two-phase flow in natural sandstone by an improved lattice Boltzmann method. *Transport in porous media* **104**, 205-229 (2014).

55 Chen, R., Shao, J.-G., Zheng, Y.-Q., Yu, H.-D. & Xu, Y.-S. Lattice Boltzmann Simulation for Complex Flow in a Solar Wall. *Communications in Theoretical Physics* **59**, 370 (2013).

56 An, S., Zhan, Y., Yao, J., Yu, H. W. & Niasar, V. A greyscale volumetric lattice Boltzmann method for upscaling pore-scale two-phase flow. *Advances in Water Resources* **144**, 103711 (2020).

57 Chen, R., Yu, H. W., Xu, Y. & Zhu, L. Scalings of inverse energy transfer and energy decay in 3-d decaying isotropic turbulence with non-rotating or rotating frame of reference. (2019).

58 Chen, R., Zeng, J. & Yu, H. W. Mechanism of damped oscillation in microbubble coalescence. *Computers & Fluids* **183**, 38-42 (2019).

59 Chen, R., Yu, H. W., Zeng, J. & Zhu, L. General power-law temporal scaling for unequal-size microbubble coalescence. *Physical Review E* **101**, 023106 (2020).

60 Jiang, F., Matsumura, K., Ohgi, J. & Chen, X. A GPU-accelerated fluid–structure-interaction solver developed by coupling finite element and lattice Boltzmann methods. *Computer Physics Communications* **259**, 107661 (2021).

61 Yu, H., Luo, L.-S. & Girimaji, S. S. Scalar mixing and chemical reaction simulations using lattice Boltzmann method. *International Journal of Computational Engineering Science* **3**, 73-87 (2002).

62 Yu, H. & Girimaji, S. S. Near-field turbulent simulations of rectangular jets using lattice Boltzmann method. *Physics of Fluids* **17**, 125106 (2005).

63 Yu, H., Girimaji, S. S. & Luo, L.-S. Lattice Boltzmann simulations of decaying homogeneous isotropic turbulence. *Physical Review E* **71**, 016708 (2005).

64 Yu, H., Girimaji, S. S. & Luo, L.-S. DNS and LES of decaying isotropic turbulence with and without frame rotation using lattice Boltzmann method. *Journal of Computational Physics* **209**, 599-616 (2005).

65 Yu, H., Li, N. & Ecke, R. E. Scaling in laminar natural convection in laterally heated cavities: is turbulence essential in the classical scaling of heat transfer? *Physical Review E* **76**, 026303 (2007).

66 Yu, H. W. *et al.* A Non-invasive Technique for Fast Assessment of Optimal LVAD Outflow Graft Implant Sites. *Circulation Research* **121**, A221-A221 (2017).

67 Sawchuk, A. P. *et al.* Noninvasive and Patient-Specific Assessment of True Severity of Renal Artery Stenosis for New Guidelines for Planning Stent Therapy. *Journal of Vascular Surgery* **68**, e64-e65 (2018).

68 Yu, H. W. *et al.* Integration of Patient-specific Computational Hemodynamics and Vessel Wall Shear Stress Into MRI Diagnosis of Vascular Diseases. *Circulation Research* **119**, A235-A235 (2016).

69 Islam, M. M., Li, H., Zhang, X., Du, X. & Yu, H. Supervised Surrogate Modeling for Hagen-Poiseuille and Womersley flows. *Bulletin of the American Physical Society* **66** (2021).

70 Jiang, F., Hirano, T., Ohgi, J. & Chen, X. A voxel image-based pulmonary airflow simulation method with an automatic detection algorithm for airway outlets. *International Journal for Numerical Methods in Biomedical Engineering* **36**, e3305 (2020).

71 Powers, K. A. & Dhamoon, A. S. Physiology, Pulmonary Ventilation and Perfusion. (2019).

72 Lasheras, J. C. The biomechanics of arterial aneurysms. *Annu. Rev. Fluid Mech.* **39**, 293-319 (2007).

73 Van Rijn, L. C. *Principles of sediment transport in rivers, estuaries and coastal seas*. Vol. 1006 (Aqua publications Amsterdam, 1993).

74 Semlitsch, B., Wang, Y. & Mihăescu, M. Flow effects due to pulsation in an internal combustion engine exhaust port. *Energy conversion and management* **86**, 520-536 (2014).

75 Womersley, J. R. Method for the calculation of velocity, rate of flow and viscous drag in arteries when the pressure gradient is known. *J Physiol* **127**, 553-563, doi:10.1113/jphysiol.1955.sp005276 (1955).

76 Sorensen, T. *et al.* in *Interspeech.* 645-649.

FINANCIAL SUPPORT

The support from the NSF grant (#1803845), Bright Focus Foundation, Extreme Science and Engineering Discovery Environment (XSEDE), supported by the NSF grant (ACI-1053575), is acknowledged for the successful completion of this work.

VITA

Md Mahfuzul Islam received a Bachelor of Science in Mechanical Engineering from Khulna University of Engineering and Technology, Bangladesh. During his Bachelor's degree, he received University Merit Scholarship for four semesters. After completing his BSc. Mr. Islam joined Upwork Inc. as an online freelancer. He joined Texas A&M University Kingsville for his Master's in Spring 2020 and later transferred to Purdue University during Fall 2020 as a recipient of Graduate Research Assistantship for the years of 2020-2022. In his Master's program, Mr. Islam has achieved a GPA of 3.57 (out of a 4.0 scale). His research achievements include two journal papers, one published and one accepted, and two conference papers (first and second author). His MS degree is expected in Spring 2022.

PUBLICATIONS

PEER-REVIEWED JOURNAL PAPERS

1. A. P. Sawchuk, W. Hong, J. Talamantes, **M. M. Islam**, Xiao Luo, Huidan Yu, The Predictive Ability of the Renal Resistive Index and its Relationship to Duplex Ultrasound Waveform Propagation in the Aorta and Renal Arteries, Annals of Vascular Surgery, (In press).
2. X. Zhang, J Gomez-Paz, J. M. McDonough, **M. M. Islam**, Y. Andreopoulos, and H. Yu*, Volumetric Lattice Boltzmann Method for Wall Stresses of Image-based Pulsatile Flows, Scientific Reports, 12, 1697 (2022).

CONFERENCE PRESENTATIONS

1. **M. M. Islam**, H. Li, H. Yu, and X. Du, Physics-Based Regression vs. CFD for Hagen-Poiseuille and Womersley Flows and Uncertainty Quantification, Eleventh International Conference on Computational Fluid Dynamics (ICCFD11), Maui, Hawaii, July 2022.
2. H. Yu, S. An, **M. M. Islam**, X. Zhang, and B. Gelfand, H. Yu, Image-based Computational Hemodynamics for Endothelium Shear Stress in Human Choriocapillaris Using Volumetric Lattice Boltzmann Method, The 74th Annual Meeting of the APS Division of Fluid Dynamics, November 21-23, 2021, Phoenix, AZ.
3. H. Yu, X. Zhang, J. Gomez, J. M. McDonough, **M.M. Islam**, and Y. Andreopoulos, GPU accelerated Volumetric Lattice Boltzmann Method for Wall Stresses in Image-based Pulsatile flows, The 17th ICMMES 2021, July 2021.

CONFERENCE POSTERS

1. W. Hong, **M.M. Islam**, J. Talamantes, A. P. Sawchuk, and H. Yu, Doppler Ultrasound Assessment of Effects on Renal Resistance of Blood Flow in Human Aortorenal Systems, The 74th Annual Meeting of the APS Division of Fluid Dynamics, 2021, Phoenix, AZ.
2. **M.M. Islam**, H. Li, X. Du, and H. Yu, Supervised Surrogate Modeling for Hagen-Poiseuille and Womersley flows, The 74th Annual Meeting of the APS Division of Fluid Dynamics, 2021.